Earth Planet. Sci. Lett. 640 (2024) 118801

Contents lists available at ScienceDirect

Earth and Planetary Science Letters

journal homepage: www.elsevier.com/locate/epsl

Simulated radiocarbon cycle revisited by considering the bipolar seesaw and benthic ^{14}C data

Peter Köhler [a,*], Luke C. Skinner [b], Florian Adolphi [a,c]

[a] Alfred-Wegener-Institut Helmholtz-Zentrum für Polar- und Meeresforschung, P.O. Box 12 01 61, Bremerhaven, 27515, Germany
[b] Godwin Laboratory for Palaeoclimate Research, Earth Sciences Department, University of Cambridge, Downing Street, Cambridge, CB2 3EQ, UK
[c] Faculty of Geosciences, University of Bremen, Klagenfurter Str. 2-4, Bremen, 28359, Germany

ARTICLE INFO

Editor: Y. Asmerom

Keywords:
radiocarbon
CO_2
AMOC
carbon cycle
model
marine reservoir age

ABSTRACT

Carbon cycle models used to calculate the marine reservoir age of the non-polar surface ocean (called Marine20) out of IntCal20, the compilation of atmospheric $\Delta^{14}C$, have so far neglected a key aspect of the millennial-scale variability connected with the thermal bipolar seesaw: changes in the strength of the Atlantic meridional overturning circulation (AMOC) related to Dansgaard/Oeschger and Heinrich events. Here we implement such AMOC changes in the carbon cycle box model BICYCLE-SE to investigate how model performance over the last 55 kyr is affected, in particular with respect to available ^{14}C and CO_2 data. Constraints from deep ocean ^{14}C data suggest that the AMOC in the model during Heinrich stadial 1 needs to be highly reduced or even completely shutdown. Ocean circulation and sea ice coverage combined are the processes that almost completely explain the simulated changes in deep ocean ^{14}C age, and these are also responsible for a glacial drawdown of ~60 ppm of atmospheric CO_2. We find that the implementation of abrupt reductions in AMOC during Greenland stadials in the model setup that was previously used for the calculation of Marine20 leads to differences of less than ±100 ^{14}C yrs. The representation of AMOC changes therefore appears to be of minor importance for deriving non-polar mean ocean radiocarbon calibration products such as Marine20, where atmospheric carbon cycle variables are forced by reconstructions. However, simulated atmospheric CO_2 exhibits minima during AMOC reductions in Heinrich stadials, in disagreement with ice core data. This mismatch supports previous suggestions that millennial-scale changes in CO_2 were probably not driven directly by the AMOC, but rather by biological and physical processes in the Southern Ocean and by contributions from variable land carbon storage.

1. Introduction

The bipolar seesaw is a well established pattern of millennial-scale climate variability found in paleo records (Stocker and Johnsen, 2003). The canonical theory to account for the bipolar seesaw states that changes in the strength of the Atlantic meridional overturning circulation (AMOC) in the ocean directly influence temperature patterns in the high latitudes. During cold periods in Greenland (so-called stadials), which are connected with a reduced AMOC, the high southern latitudes gradually warm. Rapid transitions to warm interstadials, as found in Greenland ice cores (Johnsen et al., 1992), are connected with an abrupt increase in AMOC (Henry et al., 2016) and a switch in Antarctic temperatures from gradually increasing to a gradually decreasing trend (Blunier and Brook, 2001). These variabilities describe the spatial homogeneous "oceanic mode" of the so-called Dansgaard/Oeschger (D/O) events found in Greenland ice cores which are especially well matched in Antarctic ice cores close to the Atlantic sector of the Southern Ocean (EPICA-Community-Members, 2006), while those sites further away from the Atlantic sector contain a time lag of about 200 yrs to Greenland's stadial/interstadial transitions (Buizert et al., 2018). Furthermore, a spatially heterogeneous "atmospheric mode" synchronous to abrupt changes in the north is superimposed on the signals recorded in Antarctica (Buizert et al., 2018).

While first discovered in ice cores, the connected temperature pattern of the bipolar seesaw has in the mean time been identified in various marine sediment records (e.g. Bard et al., 2000; Shackleton et al., 2000; Barker et al., 2009). Recently, a highly resolved record of sea surface temperature (SST) from the Iberian Margin has been published (Davtian and Bard, 2023) (Fig. 1a). From this record the authors were able to expand the theory of the bipolar seesaw, since

* Corresponding author.
E-mail address: peter.koehler@awi.de (P. Köhler).

https://doi.org/10.1016/j.epsl.2024.118801
Received 25 January 2024; Received in revised form 17 April 2024; Accepted 22 May 2024

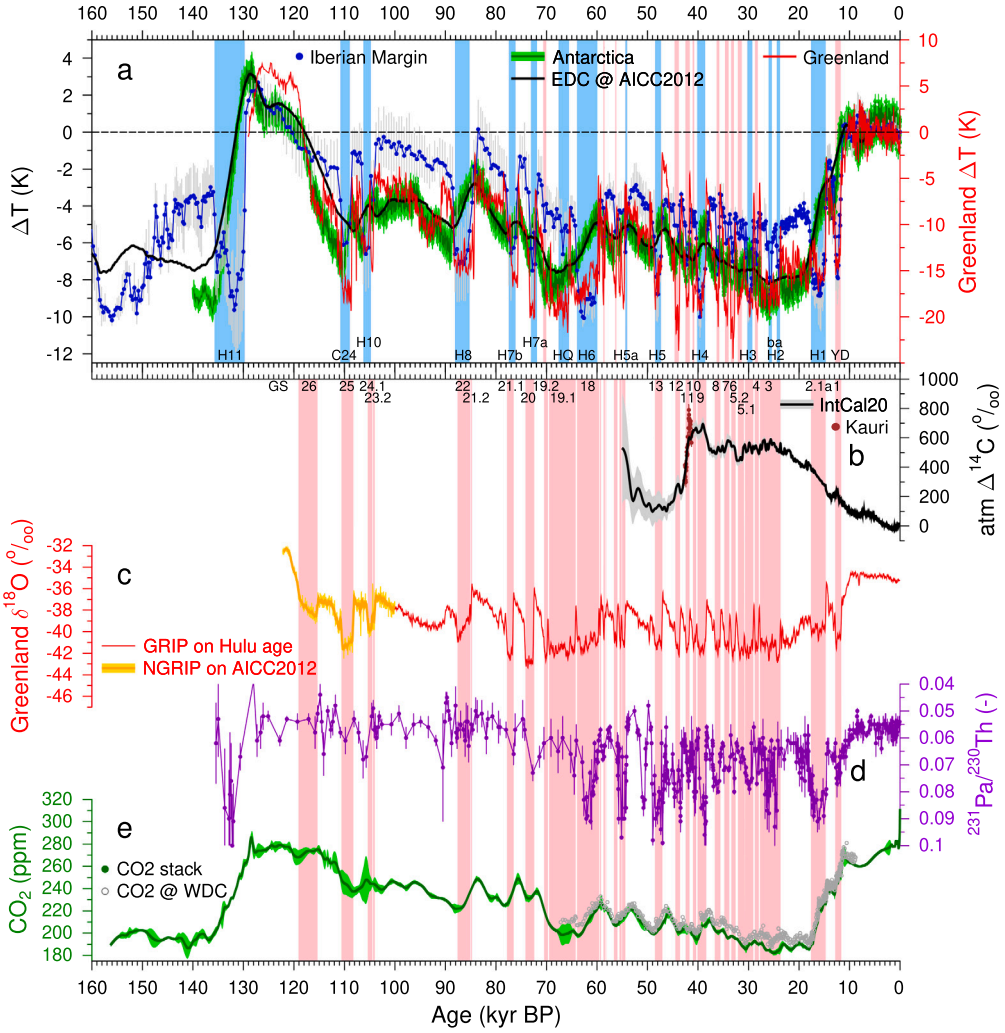

Fig. 1. Climate records across the last 160 kyr. (a) Synchronised temperature records of Greenland, Antarctica, and Iberian Margin SST as compiled in Davtian and Bard (2023). Here, we use the average of the two different Iberian Margin SST time series presented in that study. Additionally, EDC on AICC2012 as used in scenario CTRL is shown (see Fig. S2 for details). Vertical bands in mark Heinrich events (blue) or non-Heinrich stadials (pink) defined by Iberian Margin SST. Heinrich events and the Younger Dryas (YD) are labelled. (b) Atmospheric $\Delta^{14}C$ from IntCal20 (Reimer et al., 2020) and an added extension from new kauri-based data around 42 cal kBP (Cooper et al., 2021). (c) GRIP $\delta^{18}O$ on Hulu timescale and NGRIP $\delta^{18}O$ on the AICC2012 timescale (NGRIP Members, 2004). (d) $^{231}Pa/^{230}Th$ from the Bermuda rise as compiled in Lippold et al. (2019), including data from McManus et al. (2004); Böhm et al. (2015); Henry et al. (2016) on own timescale. (e) Atmospheric CO_2 (spline based on multi-records as in Köhler et al. (2017)) and a recent compilation from WDC (Bauska et al., 2021). Vertical pink bands in (b-e) mark Greenland stadials (GS, Rasmussen et al. (2014)) with their numbers shown as labels on the top ignoring GS 2.1b and 2.1c which fall into the LGM and labels for GS 15–17 (54–60 kyr BP). Greenland data in (c) are transformed on the Hulu age scale following Adolphi et al. (2018), which also contains the underlying references.

the Iberian Margin SSTs were markedly different for Greenland stadials with and without Heinrich (H) events, which are classified by ice rafted debris in North Atlantic sediment records, clearly indicating the partial disintegration of North American ice sheets (Heinrich, 1988). This distinction of Heinrich events in cold stadials (i.e. Heinrich stadials vs. non-Heinrich stadials) is not apparent in temperature or $\delta^{18}O$ data from Greenland ice cores (Fig. 1a, c), but leaves an imprint in the amplitude of temperature change in Antarctic ice core records (Margari et al., 2010; Martin et al., 2023). However, Heinrich events are important for the detailed expression of the bipolar seesaw since the AMOC is understood to be even more reduced during Heinrich stadials than during non-Heinrich stadials (Henry et al., 2016), as for example denoted by $^{231}Pa/^{230}Th$ data from the Bermuda Rise (Fig. 1d).

The importance of the bipolar seesaw and of millennial-scale changes in the AMOC on the carbon cycle is a well covered topic in simulation studies, but results are highly model-dependent (Gottschalk et al., 2019). Therefore, these abrupt AMOC changes have not yet been applied during the most recent model-based calculation of the non-polar surface ocean marine reservoir age (Marine20) forced by the IntCal20 atmospheric $\Delta^{14}C$ record (Reimer et al., 2020; Heaton et al., 2020). However, more recent analysis has shown, that the omission of millennial-scale AMOC changes might undermine the possibility to correctly simulate atmospheric $\Delta^{14}C$ when forced with independent ^{14}C production rates (Q) (Köhler et al., 2022). Furthermore, new compilations of deep ocean ^{14}C data from benthic foraminifera or deep sea corals offer now the possibility to assess applied AMOC changes via a data/model comparison of calculated deep ocean marine reservoir ages (MRAs) (Zhao et al., 2018; Skinner and Bard, 2022; Rafter et al., 2022; Skinner et al., 2023). Therefore, we here modify the most recent version of the global carbon cycle box model BICYCLE-SE (Köhler and Munhoven, 2020; Köhler and Mulitza, 2024) by implementing millennial-scale changes in AMOC and analyse how these improvements impact both simulated atmospheric CO_2 and the ^{14}C cycle during the last 55 kyr, the time window of interest for ^{14}C. Since a predecessor of BICYCLE-SE has been used to calculate Marine20, this effort allows

Table 1
Simulation scenarios. In the baseline scenarios, partly taken from Köhler et al. (2022), either atmospheric $\Delta^{14}C$, or the ^{14}C production rate (Q) is prescribed. The other variable is then derived from the model simulations. Additionally, atmospheric CO_2 is either calculated internally within the model, or prescribed from ice core data. The different AMOC scenarios are applied for all three baselines.

Acronym	Description
Baseline scenarios:	
Q1	Q constant at preindustrial level, atmospheric CO_2 and $\Delta^{14}C$ internally calculated
V1	$\Delta^{14}C$ prescribed from IntCal20 (Reimer et al., 2020), atmospheric CO_2 and Q internally calculated
V1CO2	as V1, but atmospheric CO_2 prescribed from ice core data (Köhler et al., 2017)
AMOC scenarios:	
CTRL	similar to setups in Köhler et al. (2022), no abrupt changes in AMOC connected with D/O or Heinrich events, NATL SST poorly constrained
A0	as CTRL, but improved bipolar seesaw details on SST and sea ice included
A1	as A0 + AMOC changes forced by Iberian Margin SST with 5 Sv @ H1
A2	as A0 + AMOC changes forced by Iberian Margin SST with 0 Sv @ H1
A3	as A0 + AMOC changes forced by Iberian Margin SST with 2 Sv @ H1
Ac	as A0, but AMOC constant at 16 Sv

an assessment of the current approach to dating marine records in non-polar regions using radiocarbon and the Marine20 calibration curve.

2. Methods

Throughout the study the MRA is calculated after

$$\mathrm{MRA} = 8033 \cdot \ln\left(\frac{\frac{\Delta^{14}C_{\mathrm{atmosphere}}}{1000}+1}{\frac{\Delta^{14}C_{\mathrm{sample}}}{1000}+1}\right)\ ^{14}\mathrm{C\ years} \quad (1)$$

as described in different format in Soulet et al. (2016). This equation is identical to what is used for Marine20, when the sample is the non-polar surface ocean (Heaton et al., 2020) and is equivalent to other measures of ocean-atmosphere offsets, such as B-Atm radiocarbon ages (e.g. Skinner et al., 2023), for which benthic material (fossils) is used as samples. As elaborated in detail in Skinner and Bard (2022), the magnitude and variability of the MRA depends on ocean circulation and air-sea gas exchange, as well as atmospheric $\Delta^{14}C$, and therefore on changes in Q and the carbon cycle. Therefore MRA, and (radiocarbon) 'ventilation ages', do not provide a direct measure of water mass age, as provided by theoretical 'ideal ages' or 'transit times'. Rather, MRA provides an indication of the extent of isotopic disequilibrium between a parcel of water and the contemporary atmosphere.

2.1. Model and simulation scenarios

Model: We here analyse simulation results performed with BICYCLE-SE, the Solid Earth version of the Box model of the Isotopic Carbon cYCLE (Köhler and Munhoven, 2020). In its core the model consists of a 10-box ocean, a 1-box atmosphere and a 7-box terrestrial biosphere (Fig. S1b), which has been extended by volcanic outgassing, weathering influxes as well as shallow and deep water sinks of carbonate in coral reefs and sediments (Fig. S1a). The model describes changes in the state variables of the carbon cycle (carbon content and further variables of the marine carbonate system in the ocean) and of the C isotopes ^{13}C and ^{14}C in each box as function of assumed (forced) changes in climate. The model is described in detail in Köhler and Munhoven (2020), its revised implementation of ^{13}C in Köhler and Mulitza (2024). In the application here and as already done in Köhler and Mulitza (2024) we revised the applied equatorial SST by now using the stack from Barth et al. (2018), compiled from 15 non-polar sediment cores (Fig. S2d, e). All other changing climatic boundary conditions (high latitude SST, sea ice, sea level, ocean circulation, iron fertilisation of marine biology) neglecting millennial scale variability are in scenario CTRL applied as previously, see Fig. S2 for further details. Scenario differences are described further below and summarised in Table 1.

Baselines: Although Skinner et al. (2023) offers a data perspective for the closure of the radiocarbon budget, our knowledge of both Q and of carbon cycle changes is still incomplete (Köhler et al., 2022). We therefore analyse in the following the result for three different simulation baselines: (1) Q is kept constant at preindustrial levels (baseline Q1); (2) Atmospheric $\Delta^{14}C$ is prescribed from IntCal20 (Reimer et al., 2020) (baseline V1); (3) Both atmospheric $\Delta^{14}C$ and CO_2 are prescribed from data (Köhler et al., 2017; Reimer et al., 2020) (baseline V1CO2). For both (2) and (3) the time-variable Q necessary to meet the IntCal20 data is internally calculated. Here, IntCal20's value for atmospheric $\Delta^{14}C$ for 55 kyr BP is also used for older times. Atmospheric $\Delta^{14}C$ prior to 55 kyr BP is held fixed at the value given by Intcal20 at 55 kyr BP. Approach (3) was applied during the calculation of Marine20 (Heaton et al., 2020), but bears the caveat that the mass of carbon is not conserved in the model. Baselines V1 and V1CO2 have already been investigated in Köhler et al. (2022).

AMOC scenarios: In scenario A0 only the prescribed changes in high latitude SST are improved. This involved prescribing North Atlantic SST to follow the reconstruction of Davtian and Bard (2023) from the Iberian Margin. Antarctic temperature changes derived from different ice cores on a revised age scale (see Davtian and Bard, 2023, for details on underlying data and age scale) force SST changes in the Southern Ocean. Applied changes in these surface ocean boxes are rescaled to obtain glacial/interglacial (G/IG) amplitudes of 4 K (Fig. S2e). Sea ice fractional cover is assumed to linearly follow SST changes (Fig. S2e), as is Southern Ocean vertical mixing, varying between 9 and 29 Sv and following Southern Ocean SST (Fig. S2c). This tight relation between SST, sea ice, and vertical mixing in the Southern Ocean is motivated by the process of brine rejection (e.g. Bouttes et al., 2010). Sea ice coverage in the North Atlantic box (north of 50°N) is limited to 90%, which agrees with still open ocean conditions off Norway during stadials (Sadatzki et al., 2019). This sea ice limitation is further motivated by the fact that calculated atmospheric CO_2 in carbon cycle box models is rather sensitive to nearly completely sea ice covered high latitude surface boxes largely preventing gas exchange (e.g. see Stephens and Keeling, 2000; Köhler and Fischer, 2006), a situation which leads to rather unrealistic results. In addition to the forcing applied in scenario A0, the change in North Atlantic Deep Water (NADW) formation and consequently the AMOC is also linearly prescribed by Iberian Margin SST to allow NADW to be reduced from ~10 Sv during the Last Glacial Maximum (LGM) (e.g. Meissner et al., 2003) to ~5 Sv in the Heinrich 1 stadial (scenario A1). Alternatively, most drastic (non-linear) reductions to 0 Sv and 2 Sv during Heinrich stadials are tested in scenarios A2 and A3, respectively. Here and in the following, changes in NADW strength and AMOC are used synonymously and the mentioned flux is the strength of the downwelling ocean circulation in the North Atlantic surface box (see Fig. S1b). Using Iberian Margin SST as a means of parameterising NADW is preferable to using Greenland $\delta^{18}O$ or temperature (Fig. 1a, c) since the different NADW strength in stadials with and without Heinrich events, as indicated by $^{231}Pa/^{230}Th$ at the Bermuda Rise (Fig. 1d) is not depicted in these data

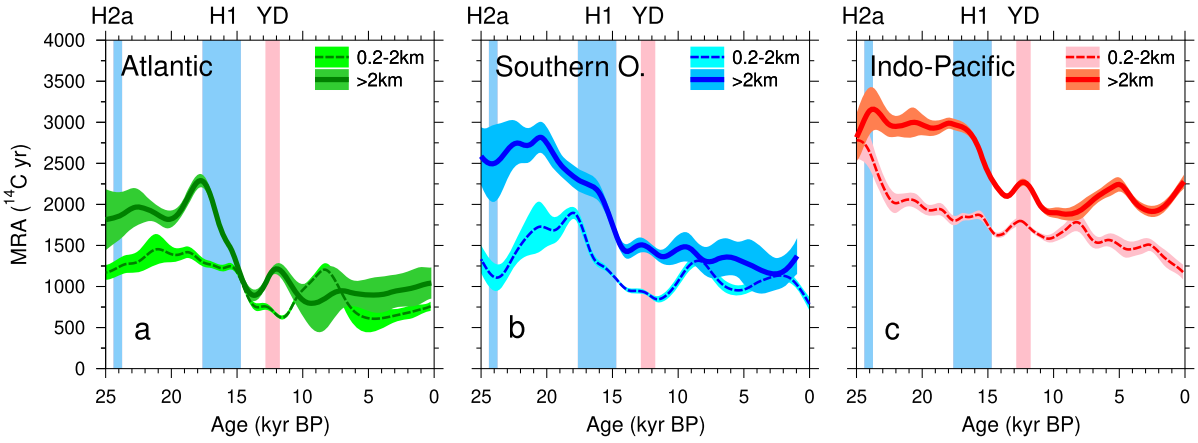

Fig. 2. Time series of absolute MRA based on benthic ^{14}C data. (a): Atlantic; (b) Southern Ocean; (c) Indo-Pacific. Differences with respect to preindustrial (PRE) as plotted in Figs. 4-5 use the last points in time series as value for PRE. This interpretation is based on the baseline selection of Skinner et al. (2023) with differences as described in the methods. Individual data points are averaged according to water depth before splines have been calculated. Uncertainties show $\pm 1\sigma$.

from Greenland. The Bermuda Rise ^{231}Pa/^{230}Th (McManus et al., 2004; Böhm et al., 2015; Henry et al., 2016; Lippold et al., 2019) is arguably a better candidate to force AMOC change; however it would need to be placed on a consistent chronology, and it is notable that when using a linear relationship of AMOC strength with Iberian Margin SST we obtain an AMOC reduction to 10 Sv at LGM, in agreement with previous parameterisation of BICYCLE-SE and with other models (Meissner et al., 2003; Pöppelmeier et al., 2023). Such a consistent outcome is not obtained when using a linear scaling of the available ^{231}Pa/^{230}Th data. Ultimately, the use of Iberian Margin SST to determine AMOC forcing in the model represents a hypothesis regarding the relative magnitude of AMOC changes between the LGM, D/O stadials/interstadials, and Heinrich stadials, which we seek to evaluate to some extent by exploring a variety of alternative AMOC scenarios. In scenario Ac the AMOC is kept constant at preindustrial strength while all other climate variables are varied as usual. Scenarios A0, A1, A2, A3, and Ac are also collectively addressed as scenarios Ax.

All six scenarios are applied for all three baselines. Simulations start at 210 kyr BP, the interglacial during Marine Isotope Stage (MIS) 7a-c, to allow time for adjustment. Radiocarbon should then be independent from initialisation around 160 kyr, the time when the Iberian Margin SST records starts. Prior to 160 kyr all forcings in scenarios Ax are identical to CTRL, whose long-term forcing across the last 800 kyr has been described in detail in Köhler and Munhoven (2020). However, since reconstructed ^{14}C is limited to ~ten times its half-lifetime of 5730 yrs, we restrict in the following our analysis to this so-called radiocarbon time window of the last 55 kyr.

2.2. Deep ocean ^{14}C data

Recently, two different approaches to analysing benthic ^{14}C data and the related MRA across the deglaciation have been published. While Rafter et al. (2022) focus on averaged time-series of MRA for different proposed "density classes" in the deep ocean (below 1 km water depth), Skinner et al. (2023) provide regional spline time-series, as well as interpolated whole ocean fields for defined time slices. Thus, both approaches are complementary to each other.

In the interpretation of deep ocean MRA of Skinner et al. (2023) the benthic Δ^{14}C data across the last 22 kyr have been assigned to six time slices (early and late Holocene, Younger Drays (YD), Bølling/Allerød (BA) Heinrich stadial 1 (HS1), LGM) in order to allow the interpolation of the data to achieve a whole ocean MRA following Skinner et al. (2017). Furthermore, three different sets of data have been analysed; we here use the baseline selection in which data with quality issues and from sites with low accumulation rate (<2 cm/kyr) have been excluded. The MRA time series based on this data selection are found for the last 25 kyr in Fig. 2, where Southern Ocean contains all cores south of 36°S, and Pacific and Indian Ocean cores are combined into one spline, similarly as boxes in the model. Splines are plotted for data from deep (>2 km) and mid-depth (0.2–2 km) cores. The splines were generated using the cubic spline function in Matlab, with a stiffness factor of 10^{-9}. Confidence intervals are based on 1000 cubic spline iterations that randomly sample the stated 1 σ-uncertainty in each ^{14}C data point. After applying the data flags reported by Skinner et al. (2023), no further data are rejected. Comparisons of our MRA time series based on Skinner et al. (2023) with the compilation presented in Rafter et al. (2022) indicate minor differences, which can be accounted for by different choices for data inclusion and construction of the splines. Key features of the benthic ^{14}C data were discussed in detail in Skinner et al. (2023).

Recently, Stott (2023) drew attention to the possibility that very high radiocarbon ventilation ages, e.g. >3,000 ^{14}C yrs in the glacial deep North Pacific as reported by Rafter et al. (2022), could reflect biases arising from the effects of bioturbation at low sedimentation rate sites. By exploring the impacts of data flags based on low/high sedimentation rates Skinner et al. (2023) found that the estimated mean ocean MRA anomaly at the LGM with respect to the preindustrial (PRE) is indeed increased from 634 to 825 ^{14}C yrs if lower sedimentation rate sites (<2 cm/kyr versus >10 cm/kyr) are included. However, it was noted that this could in part reflect a broad correlation of sedimentation rates with water depth, whereby larger radiocarbon age anomalies might occur deeper in the ocean, where lower sedimentation rates prevail. Furthermore, it was observed that the evolving spatial and temporal patterns across the last deglaciation appeared not to be significantly affected by different sedimentation rate data flags. The potential biases in radiocarbon age offsets associated with bioturbation at low sedimentation rates sites remain an important issue to resolve.

3. Results and discussions

If the AMOC is prescribed as a linear function of Iberian Margin SST (scenario A1) its strength during glacial times is reduced from the preindustrial 16 Sv to ~10 Sv, very similar to the assumed strength in the previous simulations (scenario CTRL) (Fig. 3). During stadials in the same scenario the AMOC is further reduced to 2-8 Sv, with generally larger reductions during Heinrich stadials than during non-Heinrich stadials (e.g. 5 Sv is prescribed in the H1 event). Thus, for the deglaciation the assumed AMOC in scenario A1 is approximately in agreement with that of a multi-proxy evaluation using the Bern3D model (Pöppelmeier et al., 2023). The differences between scenarios A2 or A3 (when the AMOC during Heinrich events is more strictly defined as a complete shutdown or reduced to 2 Sv, respectively) compared to A1 are specific to each individual Heinrich event. In the H4 event around 39 kyr BP,

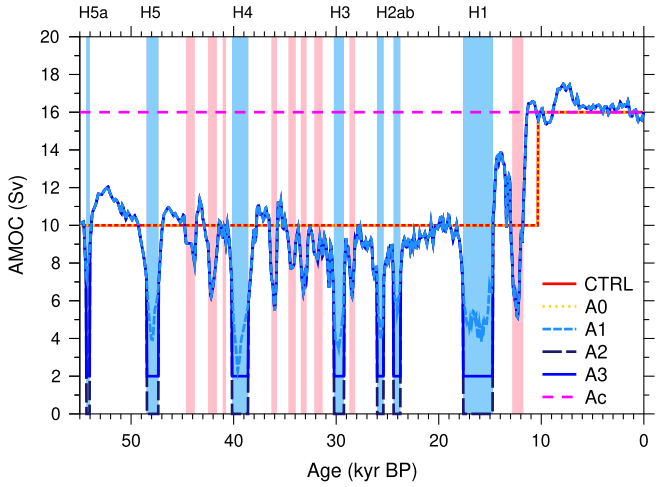

Fig. 3. Assumed AMOC changes applied in the different scenarios. Light blue bars denote Heinrich events, pink bars non-Heinrich stadials.

for example, there is hardly any difference between AMOC in scenarios A1 and A3, since the Iberian Margin SST already suggested an AMOC of only 2 Sv in scenario A1. In the following subsections we discuss the resulting effects of these prescribed AMOC changes on the various variables of interest. A condensed view on most results of each of the three baselines is compiled in the Supplemental Material (Figs. S3–S5).

3.1. Whole ocean Marine Reservoir Age

Whole ocean MRA anomalies in Skinner et al. (2023) are calculated for six time slices with respect to the natural (pre-bomb) GLODAP-based (Key et al., 2004) value of 1359 ^{14}C yrs. The width of the time slices is marked by horizontal error bars around the squares in Fig. 4a–c. We find that the preindustrial reference values in our simulations depend on the baselines, ranging from around 1100 ^{14}C yrs in Q1 (about 250 ^{14}C yrs younger than GLODAP) to 900–950 ^{14}C yrs in the simulations with variable Q (Fig. 4a–c). This offset of 150–200 ^{14}C yrs between baselines illustrates that the history of ^{14}C plays a certain role for the preindustrial ^{14}C-based age calculations, which has already been expressed by the necessity of larger than 10 kyr long spin-ups before (e.g. Köhler et al., 2006; Roth and Joos, 2013).

The benthic ^{14}C data of Skinner et al. (2023) used here suggest a ~764 ^{14}C yrs older whole ocean at LGM compared to the PRE. This MRA anomaly is reduced to ~518 ^{14}C yrs in the HS1, to ~76 ^{14}C yrs in the BA and to ~125 ^{14}C yrs in the YD followed by little MRA changes in the Holocene (Fig. 4a–c). This general pattern in whole ocean MRA is reproduced by the simulated time series, where the baselines with variable Q (V1, V1CO2, Fig. 4b, c) contain larger amplitudes in the HS1-BA-YD-Holocene zig-zag pattern than those scenarios with constant Q (Q1, Fig. 4a). These fast changes in the simulation-based whole ocean MRA cannot be reconstructed using time slice-based calculations that are averaged over multi-millennial time windows. Furthermore, in baselines V1 and V1CO2 there is a MRA anomaly peak of about 300 ^{14}C yrs in the Holocene around 7 kyr BP which is not resolved in data and which seems to be caused by changes in Q, and, as discussed in the next subsection, found in all deep ocean basins, but only to some extent resolved in data-based deep ocean MRA splines. The whole ocean MRA anomaly during the LGM is in all simulations underestimated by at least 200 ^{14}C yrs. However, in baselines V1 and V1CO2 MRA anomalies during the LGM that are comparable to the data are obtained in most scenarios directly prior to and after the time window defining the LGM time slice. This effect might be a realisation of the so-called “phase-attenuation” bias unrelated to ocean dynamics but caused by independent rapid atmospheric ^{14}C dynamics instead, as discussed in detail in Skinner et al. (2023). Alternatively, whole ocean MRA anomalies at LGM calculated from the data are only 634 ^{14}C yrs, in closer agreement with the simulations, if only sites with high sedimentation rates above 10 cm/kyr are considered (Skinner et al., 2023). The general pattern between different AMOC scenarios is that the weaker the average prescribed AMOC is the “older” the whole ocean appears in the simulations.

3.2. Deep ocean Marine Reservoir Age

Comparing simulated deep ocean MRA time series with data must be done with caution, both because of the extremely coarse resolution of the box model, and because the calculated splines will reflect the weightings that have been used in their construction (giving equal or unequal weight to signals from sparsely sampled locations). Global interpolations of simulation results demonstrated that unweighted arithmetric means using data from available core locations underestimate the global mean by ~273 ^{14}C-yrs on average (Skinner et al., 2023). Furthermore, the BICYCLE-SE model has only one deep ocean box in each of three basins which should represent waters below 1 km water depth, leaving the geometry of the main water masses unresolved. Here, we restrict the data/model comparison to the last 25 kyr. Although older data exist, they are rather coarsely distributed and with more uncertain age-control and demand further measurements before meaningful basin-wide splines might be generated. Furthermore, we use for this data/model comparison only the splines from the data below 2 km water depth. In the model the Arctic Ocean is part of the Atlantic box, while there is a paucity of data from the Arctic basin in the current data compilation. With these limitations in mind the tentative data/model comparison leads to the following insights.

The offsets between simulations and the data compilation for preindustrial times (squares in Figs. 4, 5) are of similar size for the deep Atlantic ocean time series as for the whole ocean MRA, but larger for the other ocean basins. The data suggest preindustrial MRA of 2300 (Indo-Pacific), 1100 (Atlantic), and 1400 (Southern Ocean) ^{14}C yrs, while simulated preindustrial MRA were 800–1000, 250–450, and 500–700 ^{14}C yrs smaller in Indo-Pacific, Atlantic and Southern Ocean, respectively. Again, lower simulated MRA (i.e. in larger disagreement with the data) have been obtained when Q was internally calculated to meet the IntCal20 reconstructions. These data/model offsets for preindustrial MRA are to a large extent caused by the different selection criteria that restricted deep ocean data to water depth below 2 km or more, while deep ocean boxes in the model summarised all waters deeper than 1 km.

In the deep Indo-Pacific the simulated LGM MRA anomaly of 700 ^{14}C yrs is consistent with the data (Fig. 4d–f). The HS1 decline to zero MRA anomaly seen in the Indo-Pacific data is met by the simulations as is the MRA maximum during the YD. There is a mid Holocene peak in deep Indo-Pacific MRA data which is in its dynamic roughly met, but not in absolute values and timing, by the simulation scenarios with prescribed atmosphere (baselines V1, V1CO2).

The LGM MRA anomaly of ~800 ^{14}C yrs in the deep Atlantic in the data compilation is generally met by the simulations (Fig. 5a–c). The aging of the waters in the deep Atlantic during HS1 by ~500 ^{14}C yrs in the simulations is only obtained if the AMOC is reduced to at least 2 Sv (scenario A3), or even completely shutdown (scenario A2). In simulations the deep Atlantic MRA peak is mainly restricted to HS1, while in the reconstruction the MRA rise started already at 19-20 kyr BP. As already seen for the whole ocean MRA and the deep Indo-Pacific the zig-zag-pattern of MRA across HS1-BA-YD-Holocene is better matched by simulations with variable Q (baselines V1, V1CO2). However, since it has been shown that there is no systematic D/O-related change in Q (Muscheler and Beer, 2006) our results highlight that a variable Q amplifies changes in ^{14}C, which nevertheless have their root cause in the carbon cycle (e.g. Muscheler et al., 2008). Simulations show MRA peaks for all Heinrich events in the deep Atlantic. The MRA anomalies in the data are in the Holocene rather flat, but atmospheric patterns are imprinted in the simulated deep Atlantic Ocean MRA for baselines V1 and V1CO2 with amplitudes of up to 300 ^{14}C

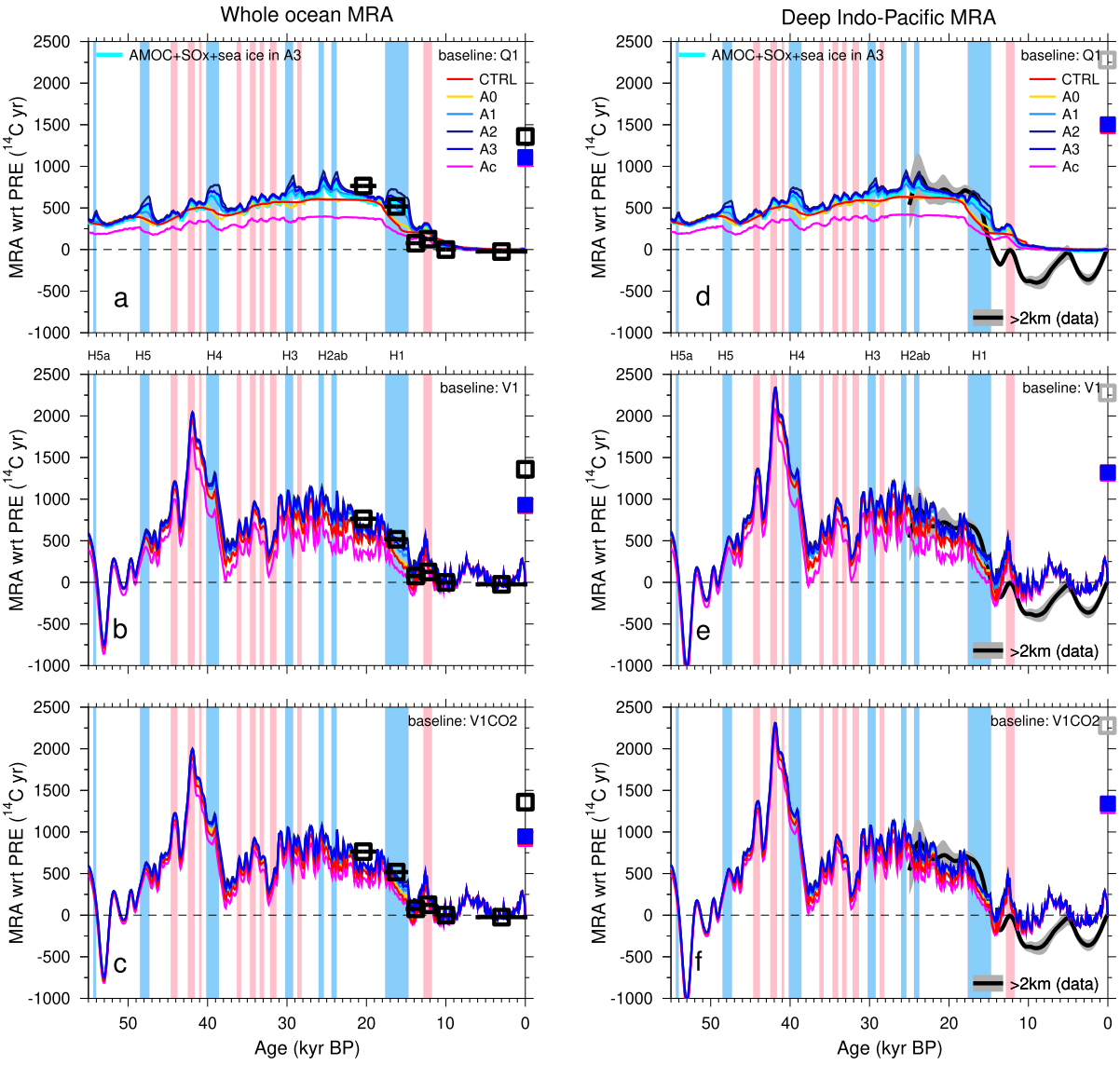

Fig. 4. MRA age for the whole ocean (a–c) and the deep Indo-Pacific (d–f) for the different baselines (first row: Q1; second row: V1; third row V1CO2) against data and the different scenarios (CTRL, A0, A1, A2, A3, Ac). The cyan-coloured lines in subfigures a, d mark the contributions of changes in AMOC, Southern Ocean vertical mixing and sea ice to the MRE in scenario A3. In (a–c) the data (open squares) are based on mean values from the analysis of six time slices in Skinner et al. (2023) where the horizontal bars depict the ranges of the time slices. Open squares around 0 kyr BP mark the preindustrial (PRE) values in the data time series from which the differences have been calculated, filled squares mark the preindustrial values in BICYCLE-SE. Light blue bars denote Heinrich events, pink bars non-Heinrich stadials.

yrs around 7 kyr BP, only weakly disagreeing with the data. From the performance of the simulated MRA anomalies in the deep Atlantic during the H1 event it appears that scenario A3 with an AMOC reduction to 2 Sv gives the closest match to observations (Fig. 5b–c). Since our suggested AMOC reduction during HS1 is much stronger than what has been obtained in Pöppelmeier et al. (2023) we tested if, alternatively, a more moderate AMOC in HS1 (scenario A1 with 5 Sv) together with a largely reduced gas exchange in the North Atlantic — realised by a 100% sea ice cover — would also lead to a comparable rise in deep Atlantic MRA. In this alternative scenario the deep Atlantic MRA differs by less than 50 ^{14}C yrs from scenario A1 and can therefore be rejected.

Simulated water ages in the deep Southern Ocean at the LGM are only ~800 ^{14}C yrs older than modern, while the data point towards ~1400 ^{14}C yrs (Fig. 5d–f). This data/model misfit with respect to the data splines is likely primarily due to the fact that these splines include data >2 km, whereas the model refers to >1 km. This view is supported by the spline through data from intermediate Southern Ocean waters which suggests 500–1000 ^{14}C years smaller ages at LGM than the deep waters (Fig. 2b). In those scenarios with abrupt AMOC changes, that agree best with deep Atlantic data, MRA anomalies in the Southern Ocean are not directly going to zero in the BA as in the data, but only to about 200 ^{14}C yrs. The positive age anomaly in the YD is in the Southern Ocean data smaller than in the Atlantic data but the simulated patterns tend to be of similar size in both basins, again more pronounced in baselines with variable Q. Stadials further back in time contain positive age anomalies of a few centuries in the simulated MRA of the Southern Ocean, but without any clear difference between Heinrich and non-Heinrich stadials. In the Holocene the simulated MRA varies only slightly and in its dynamic roughly in agreement with the reconstructions.

3.3. Surface ocean Marine Reservoir Age

Prescribing atmospheric Δ^{14}C from IntCal20, a predecessor of the model used here has been applied to derive an estimate of the mean

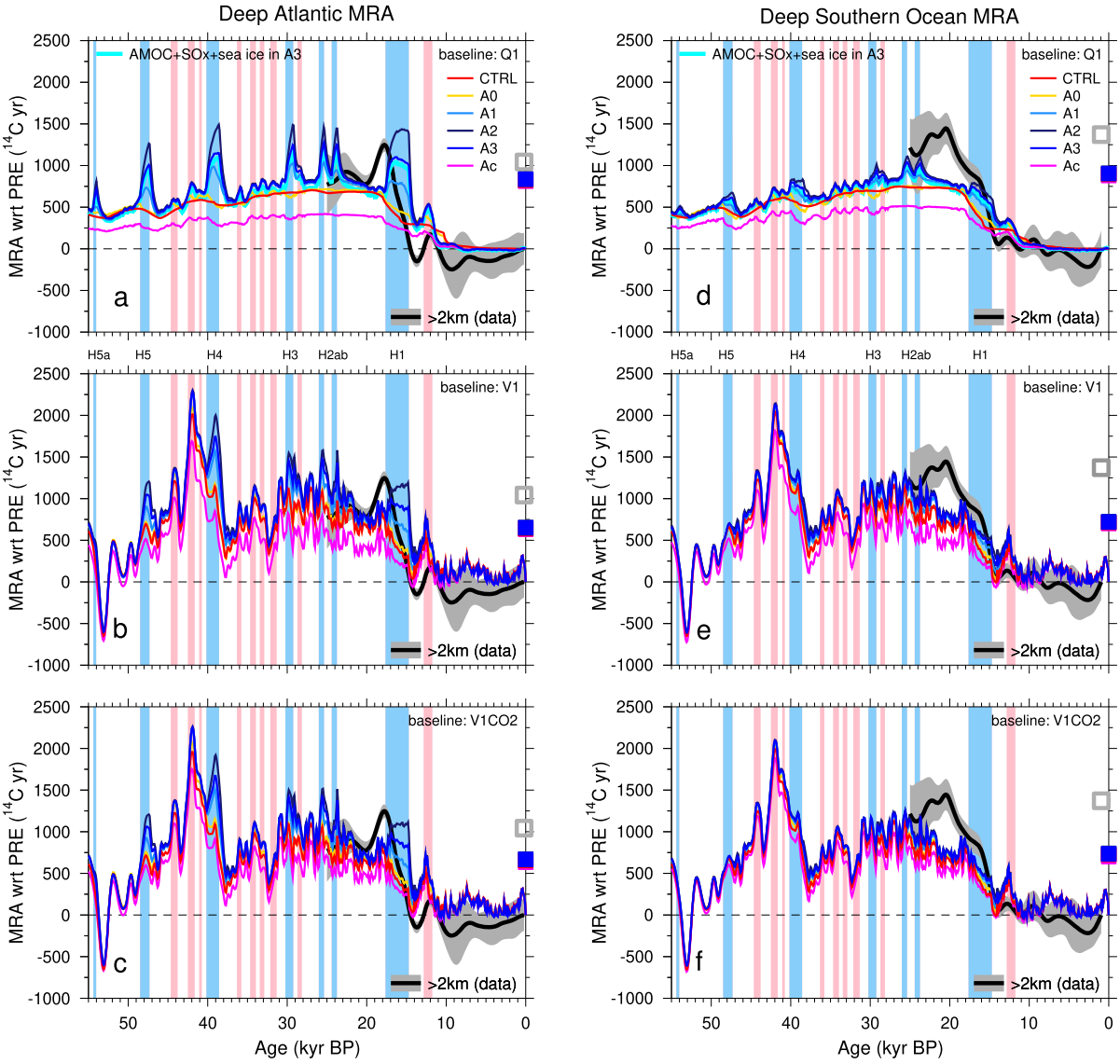

Fig. 5. MRA age in the deep Atlantic (a–c) and the deep Southern Ocean (d–f) for the different baselines (first row: Q1; second row: V1; third row V1CO2) against data and the different scenarios (CTRL, A0, A1, A2, A3, Ac). The cyan-coloured lines in subfigures a, d mark the contributions of changes in AMOC, Southern Ocean vertical mixing and sea ice to the MRE in scenario A3. Open squares around 0 kyr BP mark the preindustrial (PRE) values in the data time series from which the differences have been calculated, filled squares mark the preindustrial values in BICYCLE-SE. Light blue bars denote Heinrich events, pink bars non-Heinrich stadials.

non-polar surface MRA, or the Marine20 calibration curve (Heaton et al., 2020). Here, the non-polar surface ocean refers to the area between 40°S and 50°N in the Atlantic and 40°N in the Pacific, which contains the equatorial ocean boxes in the BICYCLE model (Fig. S1b). Our simulations provide a test of the robustness of these results, subject to the inclusion of additional carbon cycle perturbations. The simulation setup for Marine20 was similar to baseline V1CO2 in order to be as close as possible to the conditions found within the reconstructions. Our scenarios with variable AMOC for this setup show (Fig. 6c) that forcing with atmospheric data largely determines the long-term mean surface MRA output though not the global radiocarbon inventory. In other words, Marine20 is basically set by equilibrium gas exchange effects (i.e. the piston velocity, atmospheric CO_2, etc). All results lie within the uncertainty range of the 95% confidence interval (CI) of Marine20. Notably, scenario Ac with constant preindustrial AMOC strength differs mostly from the other results. Zooming in on details by calculating the difference in MRA with respect to scenario CTRL we find that the AMOC changes lead to abrupt variations in the non-polar surface ocean MRA on the order of ±100 ^{14}C yrs (Fig. 6f).

When only atmospheric $\Delta^{14}C$, but not CO_2 is prescribed from data (baseline V1) the simulated non-polar surface MRA differs more in each scenario (±150 ^{14}C yrs), although results also stay within the 95% CI of Marine20 (Fig. 6b,e). However, this is not the case anymore if none of the atmospheric carbon records are prescribed from data (baseline Q1, Fig. 6a, d). Here, only long-term trends in non-polar surface MRA are recovered (e.g. gradual increase from 750 ^{14}C yrs at 55 kyr BP to ~1000 ^{14}C yrs at LGM followed by a declining trend to 500 ^{14}C yrs at preindustrial times). Millennial-scale variations in non-polar surface MRA, including large-scale features such as the anomaly associated with high Q during the Laschamps geomagnetic excursion around 42 kyr BP (e.g. Adolphi et al., 2018; Simon et al., 2020) are largely absent, underlining that these features in Marine20 are driven by changes in Q and not by changes in the carbon cycle, at least as they are simulated here.

Altogether, these results suggest that, for the purposes of deriving an estimate of the mean non-polar surface ocean MRA from which to obtain a marine radiocarbon calibration product, the previously applied approach for Marine20 using prescribed atmospheric records (as for baseline V1CO2) is adequate. Furthermore, the outcome should remain

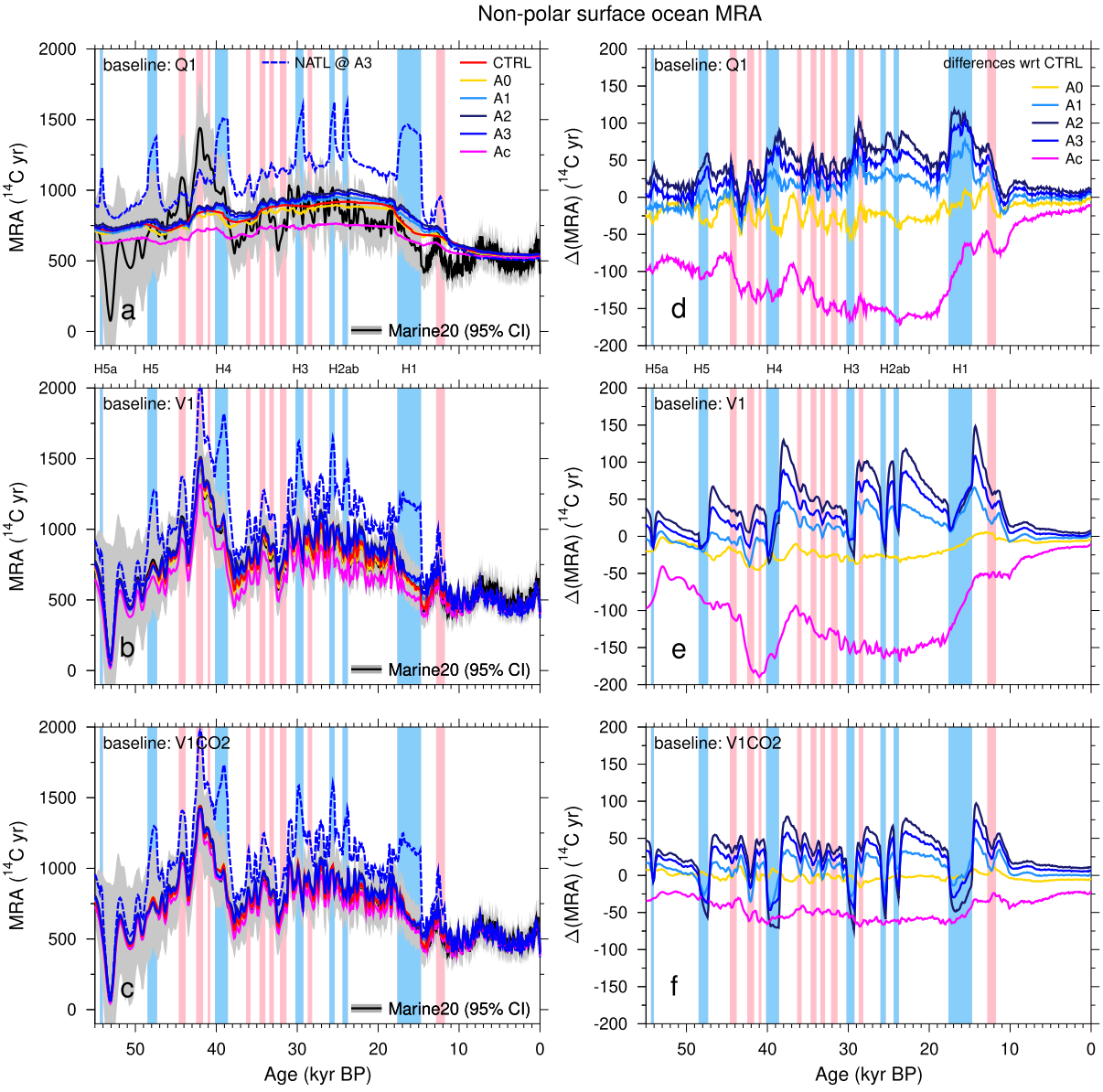

Fig. 6. Non-polar marine reservoir age for the different baselines (a: Q1; b: V1; c: V1CO2) against Marine20 (Heaton et al., 2020). Additionally, the MRA for the surface North Atlantic is shown for the most likely scenario A3. Setup similar to baseline V1CO2 (sub-figure c) and the CTRL simulation has been used for Marine20 with a predecessor version of the BICYCLE-SE model. (d–f) Changes in MRA with respect to the scenario CTRL for the three baselines. Light blue bars denote Heinrich events, pink bars non-Heinrich stadials.

robust if mass conservation in the carbon cycle simulations is desired (requiring a full forward simulation of atmospheric CO_2 for example), since only small differences arise if CO_2 is not forced by data (scenario V1).

For marine radiocarbon calibration in upwelling or polar regions variable mixed layer depth or sea ice become important factors. It is then best to either use the output from a 3D ocean general circulation model (Butzin et al., 2020) or a simplified approximation based on these results (Heaton et al., 2023). However, only lower and upper limits for MRA can so far be obtained and the impact of dynamic changes in AMOC — as investigated here for non-polar regions — is still lacking. We therefore plot as a first approximation of the temporal change in surface North Atlantic (north of 50°N) MRA results of our best-guess scenario A3 in Fig. 6. The direct comparison to data-based estimates (Stern and Lisiecki, 2013; Skinner et al., 2019) needs to be taken with caution since different areas are covered, but our results support the rise in North Atlantic surface MRA to 1000 ^{14}C yrs and above during the YD and HS1 as seen in these studies (Fig. 6c).

3.4. Atmospheric records: CO_2 and $\Delta^{14}C$

During the last deglaciation atmospheric CO_2 in ice cores rose by ~90 ppm (Köhler et al., 2017) and for the last 65 kyr (Ahn and Brook, 2014; Bauska et al., 2021) CO_2 was rising during longer (Heinrich) stadials, but changes were generally small without much coherence in the sign of change during short (non-Heinrich) stadials. In the CTRL scenario CO_2 is reduced to 180 ppm at LGM and roughly follows the long-term trends, but not the millennial-scale changes contained in the data (Fig. 7a). In detail, the simulations miss the 10–20 ppm large amplitudes found in the data and completely lack the 10 ppm variability in the LGM between H2 and H1. Introducing only the revised SST, and subsequent changes in sea ice and Southern Ocean vertical mixing (scenario A0) leads to glacial CO_2 about 10 ppm higher than in CTRL and introduces for most D/O events a variability of 5–10 ppm, more than what is actually contained in the spline through the CO_2 data (Köhler et al., 2017). If the AMOC is kept constant at 16 Sv (scenario Ac) the glacial CO_2 values are ~220 ppm, 30 ppm higher than in scenario

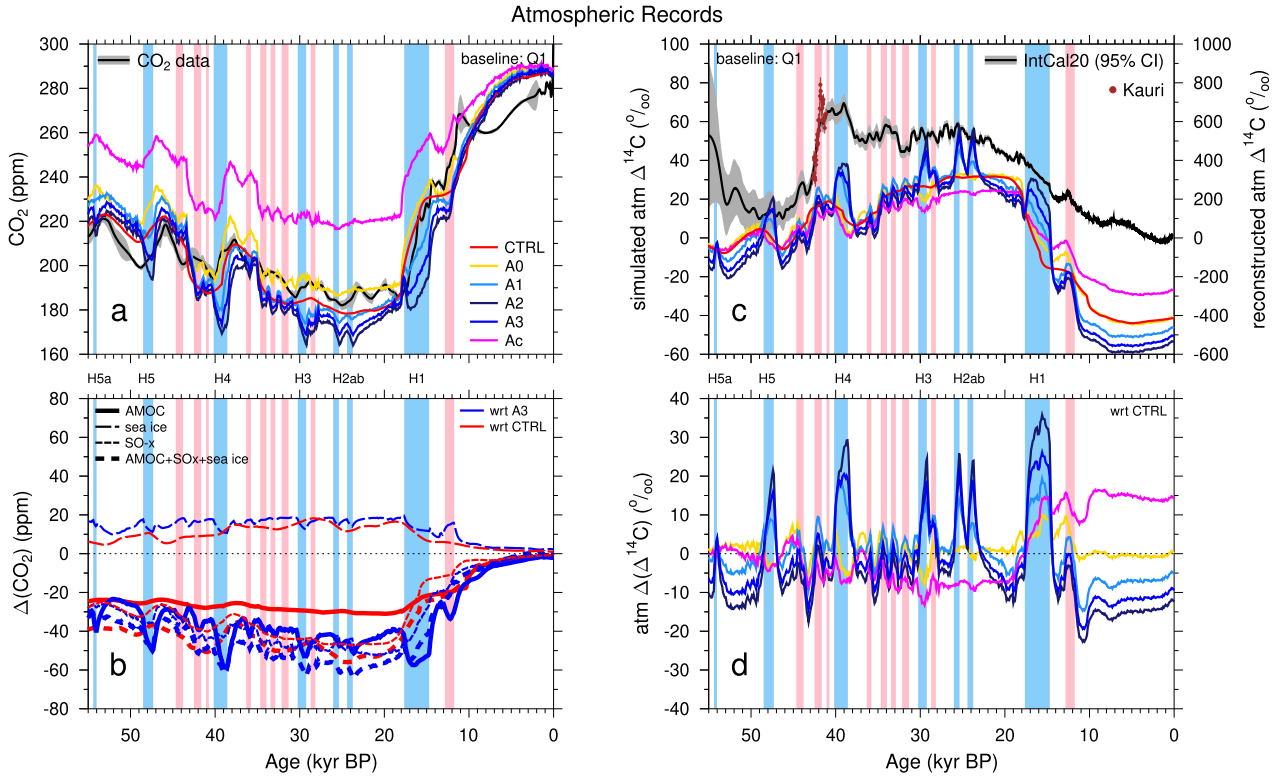

Fig. 7. Atmospheric reservoirs. (a) Internal calculated atmospheric CO_2 against data (Köhler et al., 2017). (b) Contribution of sea ice, Southern Ocean vertical mixing (SO-x) and AMOC to atmospheric CO_2 for different carbon cycle backgrounds of scenarios (CTRL: no millennial-scale AMOC changes; A3: most realistic AMOC changes). (c) Simulated atmospheric $\Delta^{14}C$ in baseline Q1 against IntCal20 reconstruction (Reimer et al., 2020) and an added extension from new kauri-based data around 42 cal kBP (Cooper et al., 2021). To allow a better comparison reconstructions are shown on different (right) y-axis which covers a factor of ten wider range. See Fig. 8 for zooms into five interesting time windows. (d) Simulated changes in atmospheric $\Delta^{14}C$ in baseline Q1 with respect to scenario CTRL. Light blue bars denote Heinrich events, pink bars non-Heinrich stadials.

A0. In the scenarios with AMOC reductions during stadials (A1, A2, A3) the simulated CO_2 during glacial times is in general reduced by 5-10 ppm compared to scenario A0, with additional reductions during Heinrich stadials of up to 20 ppm (H4 event). In summary, the opposing effects on atmospheric CO_2 from SST (and subsequent effects on sea ice and Southern Ocean vertical mixing) and AMOC anomalies imposed in the model lead in scenario A1 to values relatively close to those of the CTRL scenario. The different processes being thought to be responsible for most of the changes in deep ocean ^{14}C — ocean circulation and sea ice limiting gas exchange — add up in the most realistic scenario A3 to a rise in atmospheric CO_2 of 60 ppm since 22 kyr BP from which a dominant part of about 25 ppm is obtained during HS1 (Fig. 7b).

The isolated effect of AMOC reduction during Heinrich events always leads to CO_2 reductions in the simulations which is opposite to the ice core data. This finding has already been found with a predecessor of the BICYCLE-SE model (Köhler et al., 2006) and implies that other processes need to be responsible, which is supported by various other studies: Lacerra et al. (2017) shows enhanced carbon storage in the mid-depth Atlantic during H1 event and the YD. Some studies point to CO_2 release from the Southern Ocean associated with enhanced vertical mixing (e.g. Anderson et al., 2009; Skinner et al., 2010) or reduced biological export efficiency (e.g. Schmittner and Lund, 2015; Martínez-García et al., 2014; Lacerra et al., 2019). Others (Gottschalk et al., 2016; Anderson et al., 2024) found that the Atlantic and Pacific part of the Southern Ocean was, for both physical and biological reasons, a source of CO_2 during Greenland stadials in MIS 3.

The misfit to the CO_2 data we obtain here, especially during Heinrich events with greatly reduced AMOC is difficult to overcome and not easily solved by compensating effects derived from an increase in Southern Ocean ventilation. Thus, the simplicity of the applied box model might here come to its limits. One potentially responsible process largely underrepresented here is a change in the terrestrial carbon cycle typically related to temperature pattern of the bipolar seesaw manifested during D/O event, which is also known to depend on background climate (Köhler et al., 2005; Menviel et al., 2008). Thus, the net millennial scale CO_2 impact of abrupt AMOC changes is likely a fine balance of opposing and/or additive effects from a range of marine and terrestrial processes, which remain poorly constrained. More details on conflicting model-dependent results are summarised in Gottschalk et al. (2019).

As already shown in Köhler et al. (2006) and in other studies (e.g. Butzin et al., 2005; Muscheler et al., 2008; Meissner, 2007; Ritz et al., 2008; Singarayer et al., 2008; Hain et al., 2014) an AMOC reduction generally increases atmospheric $\Delta^{14}C$ in a model simulation (Figs. 7c, d, 8). Here, Matsumoto and Yokoyama (2013) is an exception to this rule showing declining atmospheric $\Delta^{14}C$ for an AMOC shutdown during the YD. In our setup such changes in atmospheric $\Delta^{14}C$ can only be shown for baseline Q1, since in the other setups Q is always calculated internally to meet the IntCal20 atmospheric $\Delta^{14}C$ reconstructions. The comparison to both the IntCal20 data in general and the newer higher resolved Kauri tree data around 42 kyr BP in particular (Cooper et al., 2021) clearly shows, that millennial-scale variability in atmospheric $\Delta^{14}C$ is indeed better matched by scenarios A1–A3 than in those without reduced AMOC during stadials. However, the simulated amplitudes are on the order of 10–30‰, while in the data they appear to be on the order of 50‰. The difference is explained by the low Q leading to small values in atmospheric $\Delta^{14}C$ throughout the glacial, and should improve if a higher Q is applied. However, simulated anomalies during Heinrich stadials are larger than during non-Heinrich stadials, when, in accordance with data (e.g. Böhm et al., 2015; Henry et al., 2016; Davtian and Bard, 2023) a stronger AMOC is prescribed, while no such difference exists for anomalies in IntCal20 and there are even millennial-scale

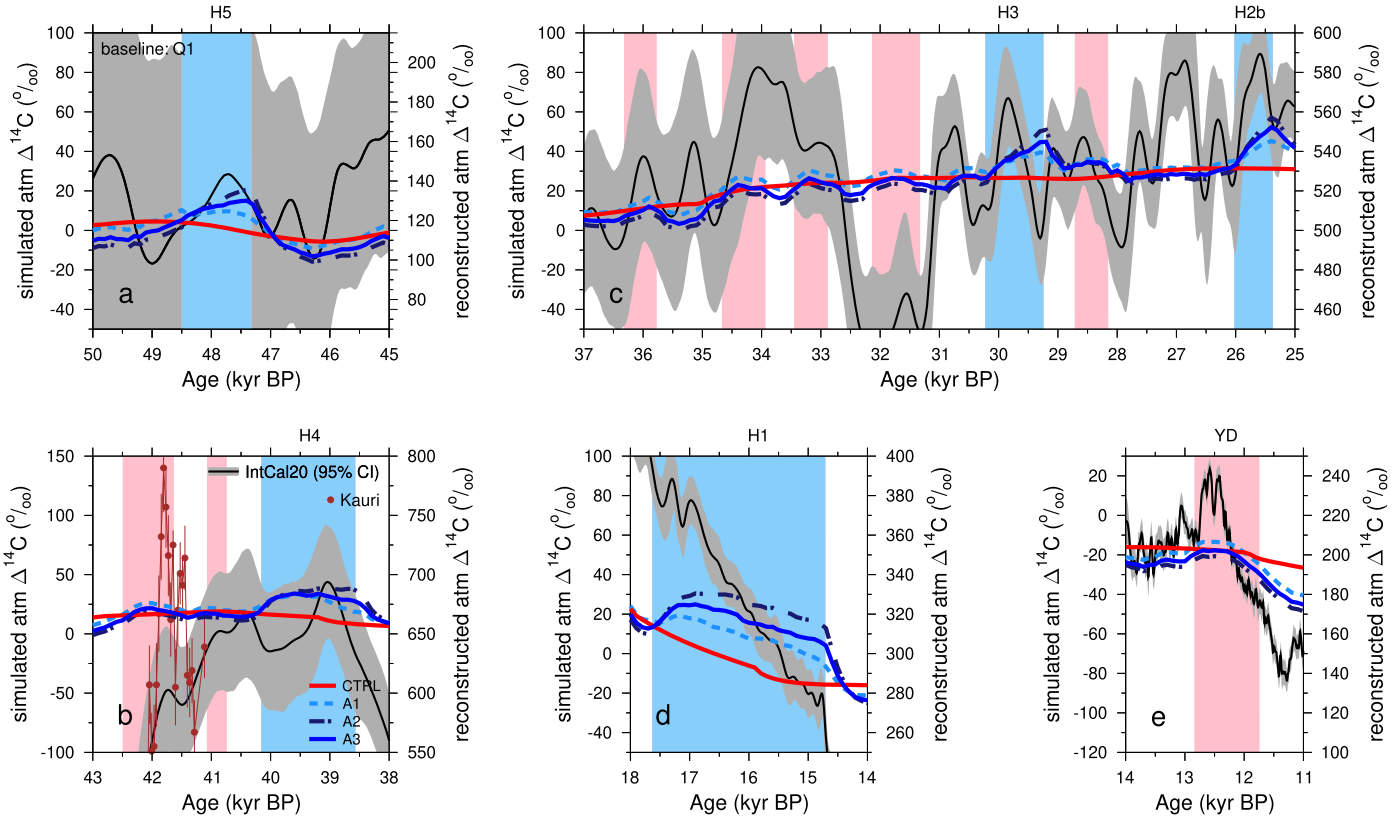

Fig. 8. Zooms on simulated and reconstructed atmospheric $\Delta^{14}C$ from IntCal20 (Reimer et al., 2020) in different time intervals. While y-axes differed between simulations and reconstructions in the plot of the full time series in Fig. 7c they show the same scales here, a range of either 250‰ (subfigure b) or of 150‰ (elsewhere). All simulations are from baseline Q1 for the four scenarios, whose labels are given in (b). Light blue bars denote Heinrich events, pink bars non-Heinrich stadials.

changes in IntCal20 without any D/O events, e.g. around 35 kyr BP (Fig. 8c).

HS1 is a special case since it is situated in Termination 1, where various other processes are assumed to change the carbon cycle as well. For example, glacial iron input into the Southern Ocean is thought to be largely reduced during the first half of the deglaciation suggesting a weakening of the biological carbon pump (Martínez-García et al., 2014) and thus potentially contributing to deglacial CO_2 rise.

Other terrestrial processes potentially impacting on atmospheric CO_2 and $\Delta^{14}C$, and not discussed any further here, are the release of petrogenic and permafrost carbon (e.g. Wu et al., 2022).

4. Conclusions

Anomalies in the deep ocean MRA are understood to be mainly caused by processes that influence the atmosphere-to-deep ocean transport of ^{14}C. In our carbon cycle model these processes are applied as changes in ocean circulation (AMOC, Southern Ocean vertical mixing) and sea ice affecting gas exchange. Other potential drivers such as wind driven gas exchange are kept constant over time in our application. Our analysis suggests that the combined effect of all these processes could indeed explain nearly all of the MRA anomalies observed in all three ocean basins (for the baseline Q1, cyan lines in Figs. 4d, 5a, d, S3). If this is correct, we can use the same simulations to identify how much atmospheric CO_2 during the last deglaciation is influenced by these processes. Or in other words, we can ask how much more carbon can an "older" glacial deep ocean store than at preindustrial times as simulated by the BICYCLE-SE box model. The ~60 ppm glacial CO_2 drawdown that the BICYCLE-SE model generates is in good agreement with the wide range of 53 ± 28 ppm based on model sensitivities using the Bern3D Earth system model of intermediate complexity (Skinner et al., 2023). Thus, more than 50% of the reconstructed G/IG CO_2 change may have had its root cause in processes that also impact ^{14}C, underlying the utility of radiocarbon as an important proxy for tracing carbon cycle change. The rest of the G/IG CO_2 change would thus be caused by other processes, especially ocean warming, but also solid Earth processes including carbonate compensation between sediments and the deep ocean while contributions from marine and terrestrial biology largely counterbalance each other (e.g. Brovkin et al., 2012; Köhler and Munhoven, 2020). While this mix of processes contributing to atmospheric CO_2 variability has long been apparent, quantified individual contributions are still model-dependent.

Meaningful reconstructions of basin-wide or whole ocean MRA are so far restricted to the last 25 kyr. Therefore, our data/model comparison was only able to judge how AMOC during HS1 might have changed, while assumptions made for earlier Heinrich events remain untested against marine ^{14}C data. Since HS1 is situated in Termination I, it might also be that the combined effects of both AMOC reduction and the massive increase in Southern Ocean ventilation (a doubling of fluxes, see Fig. S2c) leads to a specific model response, that agrees well with data, while for other Heinrich events — or more generally for other stadials — a more detailed representation of the Southern Ocean in the model and how southern sourced deep waters are generated (e.g. Menviel et al., 2014, 2018) and the consideration of variable land carbon pools (e.g. Köhler et al., 2005) might be necessary. Furthermore, the earlier onset of the rise in deep Atlantic MRA connected with HS1 in the reconstructions than in the simulations points to effects unrelated to AMOC changes or to incorrect assumptions regarding timing of AMOC changes in the model. A great deal remains to be learned regarding the impacts of D/O and Heinrich events in the carbon cycle and ^{14}C therefore.

We have shown that the imprint of abrupt AMOC changes during glacial times on the ^{14}C cycle is important and should not be ignored.

Our results also show that for the setup used to produce Marine20 — where a simple carbon cycle model is forced with atmospheric data to determine non-polar mean surface ocean MRA — AMOC changes might lead to abrupt anomalies of up to ±100 ^{14}C yrs in Marine20, which so far have been ignored. However, since these age anomalies are clearly within the given uncertainties of Marine20 our findings also confirm the robustness of the approach used to generate this mean non-polar marine calibration curve.

CRediT authorship contribution statement

Peter Köhler: Writing – review & editing, Writing – original draft, Visualization, Validation, Software, Methodology, Investigation, Formal analysis, Data curation, Conceptualization. **Luke C. Skinner:** Writing – review & editing, Software, Methodology, Funding acquisition, Formal analysis, Data curation, Conceptualization. **Florian Adolphi:** Writing – review & editing, Funding acquisition, Formal analysis, Conceptualization.

Declaration of competing interest

The authors declare that they have no known competing financial interests or personal relationships that could have appeared to influence the work reported in this paper.

Data availability

All simulation results and splines of deep ocean ^{14}C ages are available from PANGAEA (Köhler et al., 2024).

Acknowledgements

We thank N. Davtian and E. Bard for discussions and for providing data and P.U. Clark for providing the SST data connected to Barth et al. (2018). LCS is supported by NERC grant NE/V011464/1. FA is supported by the Helmholtz Association through grant no. VH-NG-1501.

Appendix A. Supplementary material

Supplementary material related to this article can be found online at https://doi.org/10.1016/j.epsl.2024.118801.

References

Adolphi, F., Bronk Ramsey, C., Erhardt, T., Edwards, R.L., Cheng, H., Turney, C.S.M., Cooper, A., Svensson, A., Rasmussen, S.O., Fischer, H., Muscheler, R., 2018. Connecting the Greenland ice-core and U/Th timescales via cosmogenic radionuclides: testing the synchroneity of Dansgaard–Oeschger events. Clim. Past 14, 1755–1781. https://doi.org/10.5194/cp-14-1755-2018.

Ahn, J., Brook, E.J., 2014. Siple Dome ice reveals two modes of millennial CO_2 change during the last ice age. Nat. Commun. 5, 3723. https://doi.org/10.1038/ncomms4723.

Anderson, H.J., Chase, Z., Bostock, H.C., Noble, T.L., Shuttleworth, R., Taiapa, B., Chen, W.H., Ren, H., Jacobsen, G.E., 2024. Millennial-scale carbon flux variability in the Subantarctic Pacific during marine isotope stage 3 (57–29 ka). Paleoceanogr. Paleoclimatol. 39, e2023PA004776. https://doi.org/10.1029/2023PA004776.

Anderson, R.F., Ali, S., Bradmiller, L.I., Nielsen, S.H.H., Fleisher, M.Q., Anderson, B.E., Burckle, L.H., 2009. Wind-driven upwelling in the Southern Ocean and the deglacial rise in atmospheric CO_2. Science 323, 1443–1448. https://doi.org/10.1126/science.1167441.

Bard, E., Rostek, F., Turon, J.L., Gendreau, S., 2000. Hydrological impact of Heinrich events in the subtropical northeast Atlantic. Science 289, 1321–1324. https://doi.org/10.1126/science.289.5483.1321.

Barker, S., Diz, P., Vantravers, M.J., Pike, J., Knorr, G., Hall, I.R., Broecker, W.S., 2009. Interhemispheric Atlantic seesaw response during the last deglaciation. Nature 457, 1007–1102. https://doi.org/10.1038/nature07770.

Barth, A.M., Clark, P.U., Bill, N.S., He, F., Pisias, N.G., 2018. Climate evolution across the mid-Brunhes transition. Clim. Past 14, 2071–2087. https://doi.org/10.5194/cp-14-2071-2018.

Bauska, T.K., Marcott, S.A., Brook, E.J., 2021. Abrupt changes in the global carbon cycle during the last glacial period. Nat. Geosci. 14, 91–96. https://doi.org/10.1038/s41561-020-00680-2.

Blunier, T., Brook, E.J., 2001. Timing of millennial-scale climate change in Antarctica and Greenland during the last glacial period. Science 291, 109–112. https://doi.org/10.1126/science.291.5501.109.

Böhm, E., Lippold, J., Gutjahr, M., Frank, M., Blaser, P., Antz, B., Fohlmeister, J., Frank, N., Andersen, M.B., Deininger, M., 2015. Strong and deep Atlantic meridional overturning circulation during the last glacial cycle. Nature 517, 73–76. https://doi.org/10.1038/nature14059.

Bouttes, N., Paillard, D., Roche, D.M., 2010. Impact of brine-induced stratification on the glacial carbon cycle. Clim. Past 6, 575–589. https://doi.org/10.5194/cp-6-575-2010.

Brovkin, V., Ganopolski, A., Archer, D., Munhoven, G., 2012. Glacial CO_2 cycle as a succession of key physical and biogeochemical processes. Clim. Past 8, 251–264. https://doi.org/10.5194/cp-8-251-2012.

Buizert, C., Sigl, M., Severi, M., Markle, B.R., Wettstein, J.J., McConnell, J.R., Pedro, J.B., Sodemann, H., Goto-Azuma, K., Kawamura, K., Fujita, S., Motoyama, H., Hirabayashi, M., Uemura, R., Stenni, B., Parrenin, F., He, F., Fudge, T.J., Steig, E.J., 2018. Abrupt ice-age shifts in southern westerly winds and Antarctic climate forced from the North. Nature 563, 681–685. https://doi.org/10.1038/s41586-018-0727-5.

Butzin, M., Heaton, T.J., Köhler, P., Lohmann, G., 2020. A short note on marine reservoir age simulations used in IntCal20. Radiocarbon 62, 865–871. https://doi.org/10.1017/RDC.2020.9.

Butzin, M., Prange, M., Lohmann, G., 2005. Radiocarbon simulations for the glacial ocean: the effects of wind stress, Southern Ocean sea ice and Heinrich events. Earth Planet. Sci. Lett. 235, 45–61. https://doi.org/10.1016/j.epsl.2005.03.003.

Cooper, A., Turney, C.S.M., Palmer, J., Hogg, A., McGlone, M., Wilmshurst, J., Lorrey, A.M., Heaton, T.J., Russell, J.M., McCracken, K., Anet, J.G., Rozanov, E., Friedel, M., Suter, I., Peter, T., Muscheler, R., Adolphi, F., Dosseto, A., Faith, J.T., Fenwick, P., Fogwill, C.J., Hughen, K., Lipson, M., Liu, J., Nowaczyk, N., Rainsley, E., Bronk Ramsey, C., Sebastianelli, P., Souilmi, Y., Stevenson, J., Thomas, Z., Tobler, R., Zech, R., 2021. A global environmental crisis 42,000 years ago. Science 371, 811–818. https://doi.org/10.1126/science.abb8677.

Davtian, N., Bard, E., 2023. A new view on abrupt climate changes and the bipolar seesaw based on paleotemperatures from Iberian Margin sediments. Proc. Natl. Acad. Sci. 120, e2209558120. https://doi.org/10.1073/pnas.2209558120.

EPICA-Community-Members, 2006. One-to-one coupling of glacial climate variability in Greenland and Antarctica. Nature 444, 195–198. https://doi.org/10.1038/nature05301.

Gottschalk, J., Battaglia, G., Fischer, H., Frölicher, T.L., Jaccard, S.L., Jeltsch-Thömmes, A., Joos, F., Köhler, P., Meissner, K.J., Menviel, L., Nehrbass-Ahles, C., Schmitt, J., Schmittner, A., Skinner, L.C., Stocker, T.F., 2019. Mechanisms of millennial-scale atmospheric CO_2 change in numerical model simulations. Quat. Sci. Rev. 220, 30–74. https://doi.org/10.1016/j.quascirev.2019.05.013.

Gottschalk, J., Skinner, L.C., Lippold, J., Vogel, H., Frank, N., Jaccard, S.L., Waelbroeck, C., 2016. Biological and physical controls in the Southern Ocean on past millennial-scale atmospheric CO_2 changes. Nat. Commun. 7, 11539. https://doi.org/10.1038/ncomms11539.

Hain, M.P., Sigman, D.M., Haug, G.H., 2014. Distinct roles of the Southern Ocean and North Atlantic in the deglacial atmospheric radiocarbon decline. Earth Planet. Sci. Lett. 394, 198–208. https://doi.org/10.1016/j.epsl.2014.03.020.

Heaton, T.J., Butzin, M., Bard, E., Bronk Ramsey, C., Hughen, K.A., Köhler, P., Reimer, P.J., 2023. Marine radiocarbon calibration in polar regions: a simple approximate approach using Marine20. Radiocarbon 65, 848–875. https://doi.org/10.1017/RDC.2023.42.

Heaton, T.J., Köhler, P., Butzin, M., Bard, E., Reimer, R.W., Austin, W.E.N., Ramsey, C.B., Grootes, P.M., Hughen, K.A., Kromer, B., Reimer, P.J., Adkins, J., Burke, A., Cook, M.S., Olsen, J., Skinner, L.C., 2020. Marine20 — the marine radiocarbon age calibration curve (0–55, 000 cal BP). Radiocarbon 62, 779–820. https://doi.org/10.1017/RDC.2020.68.

Heinrich, H., 1988. Origin and consequences of cyclic ice rafting in the northeast Atlantic Ocean during the past 130,000 years. Quat. Res. 29, 142–152. https://doi.org/10.1016/0033-5894(88)90057-9.

Henry, L.G., McManus, J.F., Curry, W.B., Roberts, N.L., Piotrowski, A.M., Keigwin, L.D., 2016. North Atlantic Ocean circulation and abrupt climate change during the last glaciation. Science 353, 470–474. https://doi.org/10.1126/science.aaf5529.

Johnsen, S.J., Clausen, H.B., Dansgaard, W., Fuhrer, K., Gundestrup, N., Hammer, C.U., Iversen, P., Jouzel, J., Stauffer, B., Steffensen, J.P., 1992. Irregular glacial interstadials recorded in a new Greenland ice core. Nature 359, 311–313. https://doi.org/10.1038/359311a0.

Key, R.M., Kozyr, A., Sabine, C.L., Lee, K., Wanninkhof, R., Bullister, J.L., Feely, R.A., Millero, F.J., Mordy, C., Peng, T.H., 2004. A global ocean carbon climatology: results from global data analysis project (GLODAP). Glob. Biogeochem. Cycles 18, GB4031. https://doi.org/10.1029/2004GB002247.

Köhler, P., Adolphi, F., Butzin, M., Muscheler, R., 2022. Toward reconciling radiocarbon production rates with carbon cycle changes of the last 55,000 years. Paleoceanogr. Paleoclimatol. 37, e2021PA004314. https://doi.org/10.1029/2021PA004314.

Köhler, P., Fischer, H., 2006. Simulating low frequency changes in atmospheric CO_2 during the last 740 000 years. Clim. Past 2, 57–78. https://doi.org/10.5194/cp-2-57-2006.

Köhler, P., Joos, F., Gerber, S., Knutti, R., 2005. Simulated changes in vegetation distribution, land carbon storage, and atmospheric CO_2 in response to a collapse of the North Atlantic thermohaline circulation. Clim. Dyn. 25, 689–708. https://doi.org/10.1007/s00382-005-0058-8.

Köhler, P., Mulitza, S., 2024. No detectable influence of the carbonate ion effect on changes in stable carbon isotope ratios ($\delta^{13}C$) of shallow dwelling planktic foraminifera over the past 160 kyr. Clim. Past 20, 991–1015. https://doi.org/10.5194/cp-20-991-2024.

Köhler, P., Munhoven, G., 2020. Late Pleistocene carbon cycle revisited by considering solid Earth processes. Paleoceanogr. Paleoclimatol. 35, e2020PA004020. https://doi.org/10.1029/2020PA004020.

Köhler, P., Muscheler, R., Fischer, H., 2006. A model-based interpretation of low frequency changes in the carbon cycle during the last 120,000 years and its implications for the reconstruction of atmospheric $\Delta^{14}C$. Geochem. Geophys. Geosyst. 7, Q11N06. https://doi.org/10.1029/2005GC001228.

Köhler, P., Nehrbass-Ahles, C., Schmitt, J., Stocker, T.F., Fischer, H., 2017. A 156 kyr smoothed history of the atmospheric greenhouse gases CO_2, CH_4, and N_2O and their radiative forcing. Earth Syst. Sci. Data 9, 363–387. https://doi.org/10.5194/essd-9-363-2017.

Köhler, P., Skinner, L.C., Adolphi, F., 2024. Splines of reconstructed deep ocean ^{14}C ages over that last 25 kyr and simulation results of the carbon and radiocarbon cycle across the last 55 kyr. PANGAEA. https://doi.org/10.1594/PANGAEA.967149.

Lacerra, M., Lund, D., Yu, J., Schmittner, A., 2017. Carbon storage in the mid-depth Atlantic during millennial-scale climate events. Paleoceanography 32, 780–795. https://doi.org/10.1002/2016PA003081.

Lacerra, M., Lund, D.C., Gebbie, G., Oppo, D.W., Yu, J., Schmittner, A., Umling, N.E., 2019. Less remineralized carbon in the intermediate-depth south Atlantic during Heinrich stadial 1. Paleoceanogr. Paleoclimatol. 34, 1218–1233. https://doi.org/10.1029/2018PA003537.

Lippold, J., Pöppelmeier, F., Süfke, F., Gutjahr, M., Goepfert, T.J., Blaser, P., Friedrich, O., Link, J.M., Wacker, L., Rheinberger, S., Jaccard, S.L., 2019. Constraining the variability of the Atlantic meridional overturning circulation during the Holocene. Geophys. Res. Lett. 46, 11338–11346. https://doi.org/10.1029/2019GL084988.

Margari, V., Skinner, L.C., Tzedakis, P.C., Ganopolski, A., Vautravers, M., Shackleton, N.J., 2010. The nature of millennial-scale climate variability during the past two glacial periods. Nat. Geosci. 3, 127–131. https://doi.org/10.1038/ngeo740.

Martin, K.C., Buizert, C., Edwards, J.S., Kalk, M.L., Riddell-Young, B., Brook, E.J., Beaudette, R., Severinghaus, J.P., Sowers, T.A., 2023. Bipolar impact and phasing of Heinrich-type climate variability. Nature 617, 100–104. https://doi.org/10.1038/s41586-023-05875-2.

Martínez-García, A., Sigman, D.M., Ren, H., Anderson, R.F., Straub, M., Hodell, D.A., Jaccard, S.L., Eglinton, T.I., Haug, G.H., 2014. Iron fertilization of the Subantarctic ocean during the last ice age. Science 343, 1347–1350. https://doi.org/10.1126/science.1246848.

Matsumoto, K., Yokoyama, Y., 2013. Atmospheric $\Delta^{14}C$ reduction in simulations of Atlantic overturning circulation shutdown. Glob. Biogeochem. Cycles 27, 296–304. https://doi.org/10.1002/gbc.20035.

McManus, J.F., Francois, R., Gheradi, J.M., Keigwin, L.D., Brown-Leger, S., 2004. Collapse and rapid resumption of Atlantic meridional circulation linked to deglacial climate changes. Nature 428, 834–837. https://doi.org/10.1038/nature02494.

Meissner, K.J., 2007. Younger Dryas: a data to model comparison to constrain the strength if the over turning circulation. Geophys. Res. Lett. 34, L21705. https://doi.org/10.1029/2007GL031304.

Meissner, K.J., Schmittner, A., Weaver, A.J., Adkins, J.F., 2003. Ventilation of the North Atlantic Ocean during the last glacial maximum: a comparison between simulated and observed radiocarbon ages. Paleoceanography 18, 1023. https://doi.org/10.1029/2002PA000762.

Menviel, L., England, M.H., Meissner, K.J., Mouchet, A., Yu, J., 2014. Atlantic-Pacific seesaw and its role in outgassing CO_2 during Heinrich events. Paleoceanography 29, 58–70. https://doi.org/10.1002/2013PA002542.

Menviel, L., Spence, P., Yu, J., Chamberlain, M.A., Matear, R.J., Meissner, K.J., England, M.H., 2018. Southern hemisphere westerlies as a driver of the early deglacial atmospheric CO_2 rise. Nat. Commun. 9, 2503. https://doi.org/10.1038/s41467-018-04876-4.

Menviel, L., Timmermann, A., Mouchet, A., Timm, O., 2008. Meridional reorganization of marine and terrestrial productivity during Heinrich events. Paleoceanography 23, PA1203. https://doi.org/10.1029/2007PA001445.

Muscheler, R., Beer, J., 2006. Solar forced Dansgaard/Oeschger events? Geophys. Res. Lett. 33, L20706. https://doi.org/10.1029/2006GL026779.

Muscheler, R., Kromer, B., Björck, S., Svensson, A., Friedrich, M., Kaiser, K.F., Southon, J., 2008. Tree rings and ice cores reveal ^{14}C calibration uncertainties during the Younger Dryas. Nat. Geosci. 1, 263–267. https://doi.org/10.1038/ngeo128.

NGRIP Members, 2004. High-resolution record of northern hemisphere climate extending into the last interglacial period. Nature 431, 147–151. https://doi.org/10.1038/nature02805.

Pöppelmeier, F., Jeltsch-Thömmes, A., Lippold, J., Joos, F., Stocker, T.F., 2023. Multiproxy constraints on Atlantic circulation dynamics since the last ice age. Nat. Geosci. 16, 349–356. https://doi.org/10.1038/s41561-023-01140-3.

Rafter, P.A., Gray, W.R., Hines, S.K., Burke, A., Costa, K.M., Gottschalk, J., Hain, M.P., Rae, J.W., Southon, J.R., Walczak, M.H., Yu, J., Adkins, J.F., DeVries, T., 2022. Global reorganization of deep-sea circulation and carbon storage after the last ice age. Sci. Adv. 8, eabq5434. https://doi.org/10.1126/sciadv.abq5434.

Rasmussen, S.O., Bigler, M., Blockley, S.P., Blunier, T., Buchardt, S.L., Clausen, H.B., Cvijanovic, I., Dahl-Jensen, D., Johnsen, S.J., Fischer, H., Gkinis, V., Guillevic, M., Hoek, W.Z., Lowe, J.J., Pedro, J.B., Popp, T., Seierstad, I.K., Steffensen, J.P., Svensson, A.M., Vallelonga, P., Vinther, B.M., Walker, M.J., Wheatley, J.J., Winstrup, M., 2014. A stratigraphic framework for abrupt climatic changes during the Last Glacial period based on three synchronized Greenland ice-core records: refining and extending the INTIMATE event stratigraphy. Quat. Sci. Rev. 106, 14–28. https://doi.org/10.1016/j.quascirev.2014.09.007.

Reimer, P.J., Austin, W.E.N., Bard, E., Bayliss, A., Blackwell, P.G., Bronk Ramsey, C., Butzin, M., Cheng, H., Edwards, R.L., Friedrich, M., Grootes, P.M., Guilderson, T.P., Hajdas, I., Heaton, T.J., Hogg, A.G., Hughen, K.A., Kromer, B., Manning, S.W., Muscheler, R., Palmer, J.G., Pearson, C., van der Plicht, H., Reimer, R.W., Richards, D.A., Scott, E.M., Southon, J.R., Turney, C.S.M., Wacker, L., Adophi, F., Büntgen, U., Capano, M., Fahrni, S., Fogtmann-Schulz, A., Friedrich, R., Köhler, P., Kudsk, S., Miyake, F., Olsen, J., Reinig, F., Sakamoto, M., Sookdeo, A., Talamo, S., 2020. The IntCal20 Northern Hemisphere radiocarbon age calibration curve (0–55 cal kBP). Radiocarbon 62, 725–757. https://doi.org/10.1017/RDC.2020.41.

Ritz, S.P., Stocker, T.F., Müller, S.A., 2008. Modelling the effect of abrupt ocean circulation change on marine reservoir age. Earth Planet. Sci. Lett. 268, 202–211. https://doi.org/10.1016/j.epsl.2008.01.024.

Roth, R., Joos, F., 2013. A reconstruction of radiocarbon production and total solar irradiance from the Holocene ^{14}C and CO_2 records: implications of data and model uncertainties. Clim. Past 9, 1879–1909. https://doi.org/10.5194/cp-9-1879-2013.

Sadatzki, H., Dokken, T.M., Berben, S.M.P., Muschitiello, F., Stein, R., Fahl, K., Menviel, L., Timmermann, A., Jansen, E., 2019. Sea ice variability in the southern Norwegian sea during glacial Dansgaard-Oeschger climate cycles. Sci. Adv. 5, eaau6174. https://doi.org/10.1126/sciadv.aau6174.

Schmittner, A., Lund, D.C., 2015. Early deglacial Atlantic overturning decline and its role in atmospheric CO_2 rise inferred from carbon isotopes ($\delta^{13}C$). Clim. Past 11, 135–152. https://doi.org/10.5194/cp-11-135-2015.

Shackleton, N.J., Hall, M.A., Vincent, E., 2000. Phase relationships between millennial-scale events 64,000–24,000 years ago. Paleoceanography 15, 565–569. https://doi.org/10.1029/2000PA000513.

Simon, Q., Thouveny, N., Bourlès, D.L., Valet, J.P., Bassinot, F., 2020. Cosmogenic ^{10}Be production records reveal dynamics of geomagnetic dipole moment (GDM) over the Laschamp excursion (20–60 ka). Earth Planet. Sci. Lett. 550, 116547. https://doi.org/10.1016/j.epsl.2020.116547.

Singarayer, J.S., Richards, D.A., Ridgwell, A., Valdes, P.J., Austin, W.E.N., Beck, J.W., 2008. An oceanic origin for the increase of atmospheric radiocarbon during the Younger Dryas. Geophys. Res. Lett. 35, L14707. https://doi.org/10.1029/2008GL034074.

Skinner, L.C., Bard, E., 2022. Radiocarbon as a dating tool and tracer in paleoceanography. Rev. Geophys. 60, e2020RG000720. https://doi.org/10.1029/2020RG000720.

Skinner, L.C., Fallon, S., Waelbroeck, C., Michel, E., Barker, S., 2010. Ventilation of the deep Southern Ocean and deglacial CO_2 rise. Science 328, 1147–1151. https://doi.org/10.1126/science.1183627.

Skinner, L.C., Muschitiello, F., Scrivner, A.E., 2019. Marine reservoir age variability over the last deglaciation: implications for marine carbon cycling and prospects for regional radiocarbon calibrations. Paleoceanogr. Paleoclimatol. 34, 1807–1815. https://doi.org/10.1029/2019PA003667.

Skinner, L.C., Primeau, F., Freeman, E., de la Fuente, M., Goodwin, P.A., Gottschalk, J., Huang, E., McCave, I.N., Noble, T.L., Scrivner, A.E., 2017. Radiocarbon constraints on the glacial ocean circulation and its impact on atmospheric CO_2. Nat. Commun. 8, 16010. https://doi.org/10.1038/ncomms16010.

Skinner, L.C., Primeau, F., Letsch-Thömmes, A., Joos, F., Köhler, P., Bard, E., 2023. Rejuvenating the ocean: mean ocean radiocarbon, CO_2 release, and radiocarbon budget closure across the last deglaciation. Clim. Past 19, 2177–2202. https://doi.org/10.5194/cp-19-2177-2023.

Soulet, G., Skinner, L.C., Beaupré, S.R., Galy, V., 2016. A note on reporting of reservoir ^{14}C disequilibria and age offsets. Radiocarbon 58, 205–211. https://doi.org/10.1017/RDC.2015.22.

Stephens, B.B., Keeling, R.F., 2000. The influence of Antarctic sea ice on glacial-interglacial CO_2 variations. Nature 404, 171–174. https://doi.org/10.1038/35004556.

Stern, J.V., Lisiecki, L.E., 2013. North Atlantic circulation and reservoir age changes over the past 41,000 years. Geophys. Res. Lett. 40, 3693–3697. https://doi.org/10.1002/grl.50679.

Stocker, T.F., Johnsen, S.J., 2003. A minimum thermodynamic model for the bipolar seesaw. Paleoceanography 18, 1087. https://doi.org/10.1029/2003PA000920.

Stott, L., 2023. How old is too old? Implications of averaging ^{14}C-based estimates of ventilation age to assess the Pacific Ocean's role in sequestering CO_2 in the past. Quat. Sci. Rev. 310, 108122. https://doi.org/10.1016/j.quascirev.2023.108122.

Wu, J., Mollenhauer, G., Stein, R., Köhler, P., Hefter, J., Fahl, K., Grotheer, H., Wei, B., Nam, S.I., 2022. Deglacial release of petrogenic and permafrost carbon from the Canadian Arctic impacting the carbon cycle. Nat. Commun. 13, 7172. https://doi.org/10.1038/s41467-022-34725-4.

Zhao, N., Marchal, O., Keigwin, L., Amrhein, D., Gebbie, G., 2018. A synthesis of deglacial deep-sea radiocarbon records and their (in)consistency with modern ocean ventilation. Paleoceanogr. Paleoclimatol. 33, 128–151. https://doi.org/10.1002/2017PA003174.

Supplementary Materials for *Simulated radiocarbon cycle revisited by considering the bipolar seesaw and benthic ^{14}C data*

Peter Köhler[a,*], Luke C. Skinner[b], Florian Adolphi[a,c]

[a] *Alfred-Wegener-Institut Helmholtz-Zentrum für Polar-und Meeresforschung (AWI), P.O. Box 12 01 61, Bremerhaven, 27515, Germany*
[b] *Godwin Laboratory for Palaeoclimate Research, Earth Sciences Department, University of Cambridge, Downing Street, Cambridge, CB2 3EQ, U.K.*
[c] *Faculty of Geosciences, University of Bremen, Klagenfurter Str. 2-4, Bremen, 28359, Germany*

Content

- References used in this Supplementary.
- Figures S1–S5.

References

Bintanja, R., van de Wal, R.S.W., 2008. North American ice-sheet dynamics and the onset of the 100,000-year glacial cycles. Nature 454, 869–872. http://doi.org/10.1038/nature07158.

Davtian, N., Bard, E., 2023. A new view on abrupt climate changes and the bipolar seesaw based on paleotemperatures from Iberian Margin sediments. Proceedings of the National Academy of Sciences 120, e2209558120. http://doi.org/10.1073/pnas.2209558120.

EPICA-community-members, 2004. Eight glacial cycles from an Antarctic ice core. Nature 429, 623–628. http://doi.org/10.1038/nature02599.

Flower, B.P., Oppo, D.W., McManus, J.F., Venz, K.A., Hodell, D.A., Cullen, J.L., 2000. North Atlantic intermediate to deep water circulation and chemical stratification during the past 1 Myr. Paleoceanography 15, 388–403. http://doi.org/10.1029/1999PA000430.

Jouzel, J., Masson-Delmotte, V., Cattani, O., Dreyfus, G., Falourd, S., Hoffmann, G., Minster, B., Nouet, J., Barnola, J.M., Chappellaz, J., Fischer, H., Gallet, J.C., Johnsen, S., Leuenberger, M., Loulergue, L., Luethi, D., Oerter, H., Parrenin, F., Raisbeck, G., Raynaud, D., Schilt, A., Schwander, J., Selmo, E., Souchez, R., Spahni, R., Stauffer, B., Steffensen, J.P., Stenni, B., Stocker, T.F., Tison, J.L., Werner, M., Wolff, E.W., 2007. Orbital and millennial Antarctic climate variability over the last 800 000 years. Science 317, 793–796. http://doi.org/10.1126/science.1141038.

Köhler, P., Fischer, H., Munhoven, G., Zeebe, R.E., 2005. Quantitative interpretation of atmospheric carbon records over the last glacial termination. Global Biogeochemical Cycles 19, GB4020. http://doi.org/10.1029/2004GB002345.

Köhler, P., Fischer, H., Schmitt, J., 2010. Atmospheric $\delta^{13}CO_2$ and its relation to pCO_2 and deep ocean $\delta^{13}C$ during the late Pleistocene. Paleoceanography 25, PA1213. http://doi.org/10.1029/2008PA001703.

*Corresponding author
Email address: peter.koehler@awi.de (Peter Köhler)

Köhler, P., Nehrbass-Ahles, C., Schmitt, J., Stocker, T.F., Fischer, H., 2017. A 156 kyr smoothed history of the atmospheric greenhouse gases CO_2, CH_4, and N_2O and their radiative forcing. Earth System Science Data 9, 363–387. http://doi.org/10.5194/essd-9-363-2017.

McManus, J.F., Oppo, D.W., Cullen, J.L., 1999. A 0.5-million-year record of millennial-scale climate variability in the North Atlantic. Science 283, 971–975. http://doi.org/10.1126/science.283.5404.971.

Reimer, P.J., Austin, W.E.N., Bard, E., Bayliss, A., Blackwell, P.G., Bronk Ramsey, C., Butzin, M., Cheng, H., Edwards, R.L., Friedrich, M., Grootes, P.M., Guilderson, T.P., Hajdas, I., Heaton, T.J., Hogg, A.G., Hughen, K.A., Kromer, B., Manning, S.W., Muscheler, R., Palmer, J.G., Pearson, C., van der Plicht, H., Reimer, R.W., Richards, D.A., Scott, E.M., Southon, J.R., Turney, C.S.M., Wacker, L., Adophi, F., Büntgen, U., Capano, M., Fahrni, S., Fogtmann-Schulz, A., Friedrich, R., Köhler, P., Kudsk, S., Miyake, F., Olsen, J., Reinig, F., Sakamoto, M., Sookdeo, A., Talamo, S., 2020. The IntCal20 Northern Hemisphere radiocarbon age calibration curve (0–55 cal kBP). Radiocarbon 62, 725–757. http://doi.org/10.1017/RDC.2020.41.

Skinner, L.C., Primeau, F., Letsch-Thömmes, A., Joos, F., Köhler, P., Bard, E., 2023. Rejuvenating the ocean: mean ocean radiocarbon, CO_2 release, and radiocarbon budget closure across the last deglaciation. Climate of the Past 19, 2177–2202. http://doi.org/10.5194/cp-19-2177-2023.

Wright, A.K., Flower, B.P., 2002. Surface and deep ocean circulation in the subpolar North Atlantic during the mid-Pleistocene revolution. Paleoceanography 17, 1068. http://doi.org/10.1029/2002PA000782.

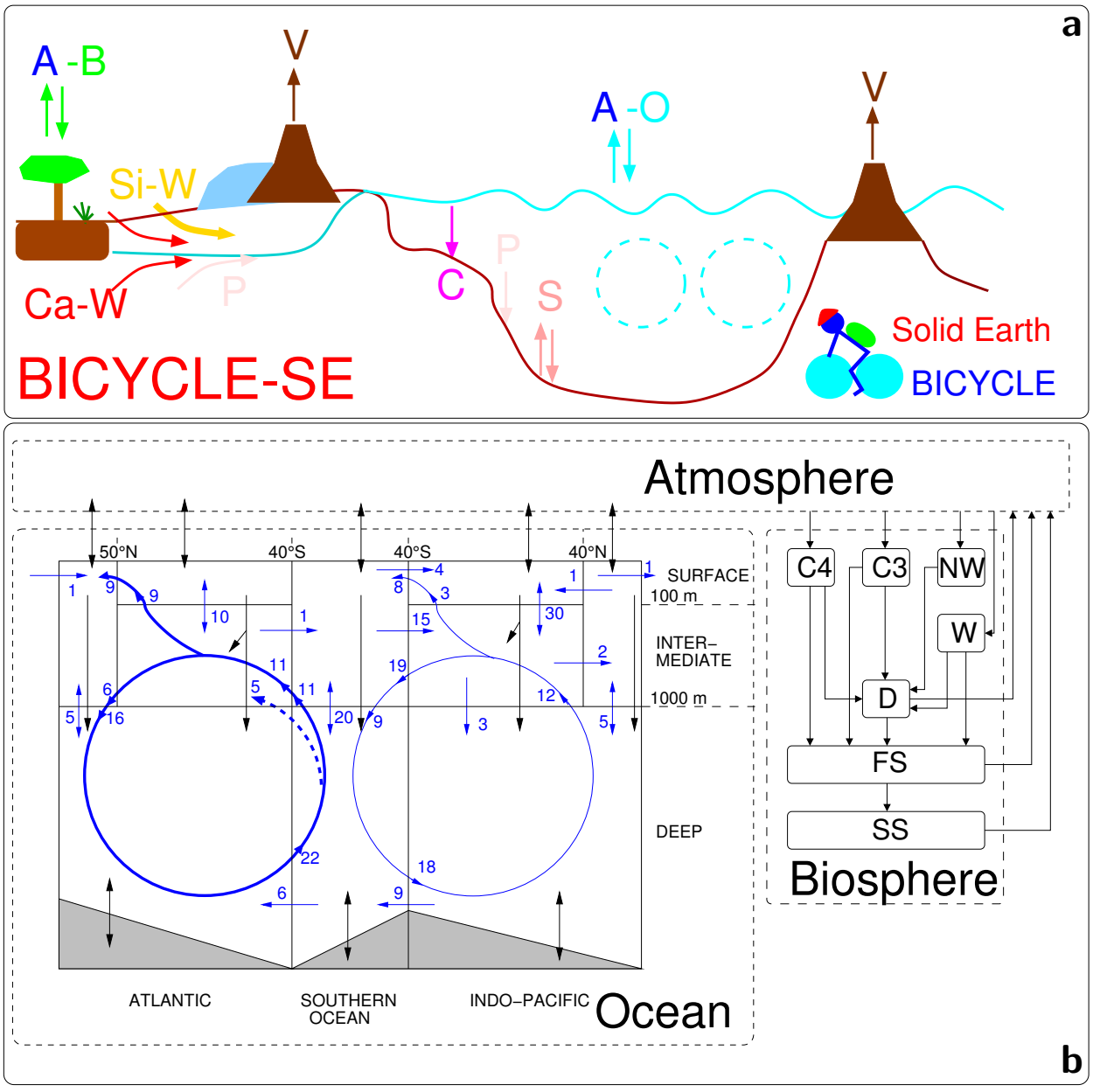

Figure S1: Sketch of the model BICYCLE-SE. (a): Overall sketch of the solid Earth fluxes. V: outgassing of CO_2 from volcanoes on land potentially and temporally overlain by land ice and from hot spot island volcanoes (and mid ocean ridges, not shown) influenced by changing sea level; C: shallow water carbonate deposition due to coral reef growth; Si-W: silicate weathering and Ca-W: carbonate weathering with different sources of C, but both delivering HCO_3^--ions into the ocean; P: PO_4^{3-} riverine input and sedimentary burial; S: $CaCO_3$ sedimentation and dissolution. A-B: atmosphere-biosphere exchange of CO_2; A-O: atmosphere-ocean exchange of CO_2. The cyan-coloured broken circles mimic the two overturning cell in the Atlantic and Indo-Pacific Ocean. The previous model version has been restricted to the fluxes A-O, A-B, and some simplified representation of carbonate compensation between ocean and sediment. (b): Details of subsystem AOB (Köhler et al., 2010) with the prescribed pre-industrial water fluxes in the ocean (blue, numbers in Sv). Bold blue circle and lines denotes fluxes connected to the AMOC. Black arrows denote carbon fluxes. The terrestrial biosphere contains: C4: C_4 ground vegetation; C3: C_3 ground vegetation; NW: non-woody parts of trees; W: woody parts of trees; D: detritus or above-ground litter; FS: fast decomposing soil or below-ground litter; SS: slow decomposing soil.

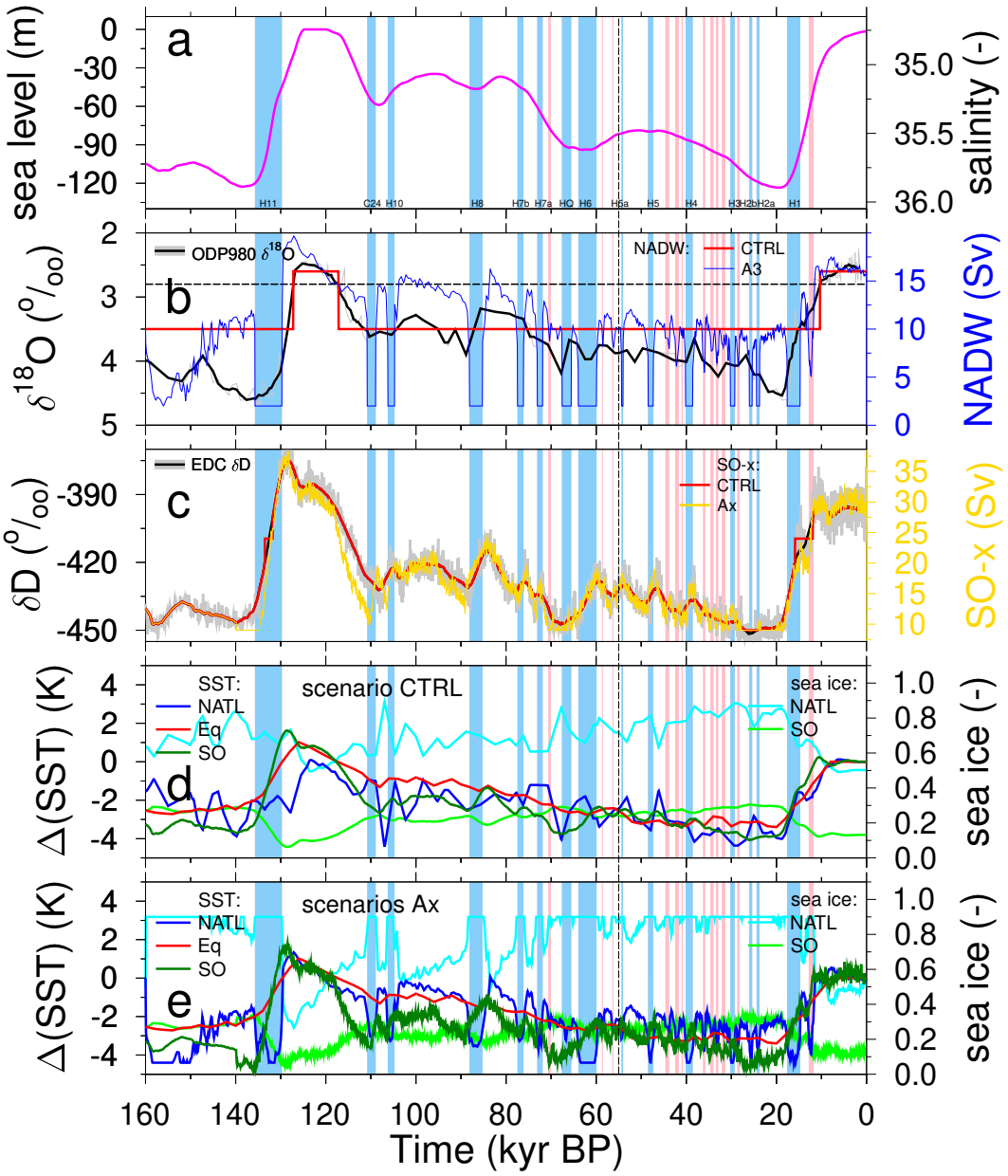

Figure S2: Time-dependent forcing of the model. (a) Sea level following Bintanja and van de Wal (2008) resulting in mean ocean salinity changes (right y-axis). (b) North Atlantic Deep Water (NADW) formation is in scenario CTRL either in interglacial or glacial mode, following δ^{18}O in OPD980 (55°29′ N, 14°42′ W) (McManus et al., 1999; Flower et al., 2000; Wright and Flower, 2002), dotted line marks the threshold for switching between both states. Rescaled summer SST data from ODP980 included in the same references is also used to force North Atlantic SST in scenario CTRL. In scenarios Ax NADW and subsequently AMOC follow Iberian Margin SST, here plotted for the example of A3. (c) EDC ice core δD (EPICA-community-members, 2004; Jouzel et al., 2007) corrected for $\delta^{18}O_{sw}$, from which Southern Ocean sea surface temperatures (SST) and vertical mixing (SO-x: SO surface-to-deep ocean flux, right y-axis) is calculated in scenario CTRL. The running mean of the corrected δD and SO-x differ during terminations, since abrupt changes in SO-x have been proposed (Köhler et al., 2005). Furthermore, a minimum for SO-x of 9 Sv is prescribed leading to small differences between long-term forcing and SO-x around 27 kyr BP. In scenarios Ax the Antarctic stack with revised age scale as published in Davtian and Bard (2023) is taken. (d-e) Changes in SST for North Atlantic (NATL), equatorial areas (Eq) and the Southern Ocean (SO) (left y-axes) and the corresponding fraction of sea ice coverage in the high latitude boxes (right y-axes) for (d) scenario CTRL and (e) scenarios Ax. The vertical line at 55 kyr BP marks the onset of the time period of interest for ^{14}C, for which results are discussed here. Vertical bands mark labelled Heinrich events (blue) or non-Heinrich stadials (pink) defined by Iberian Margin SST (Davtian and Bard, 2023).

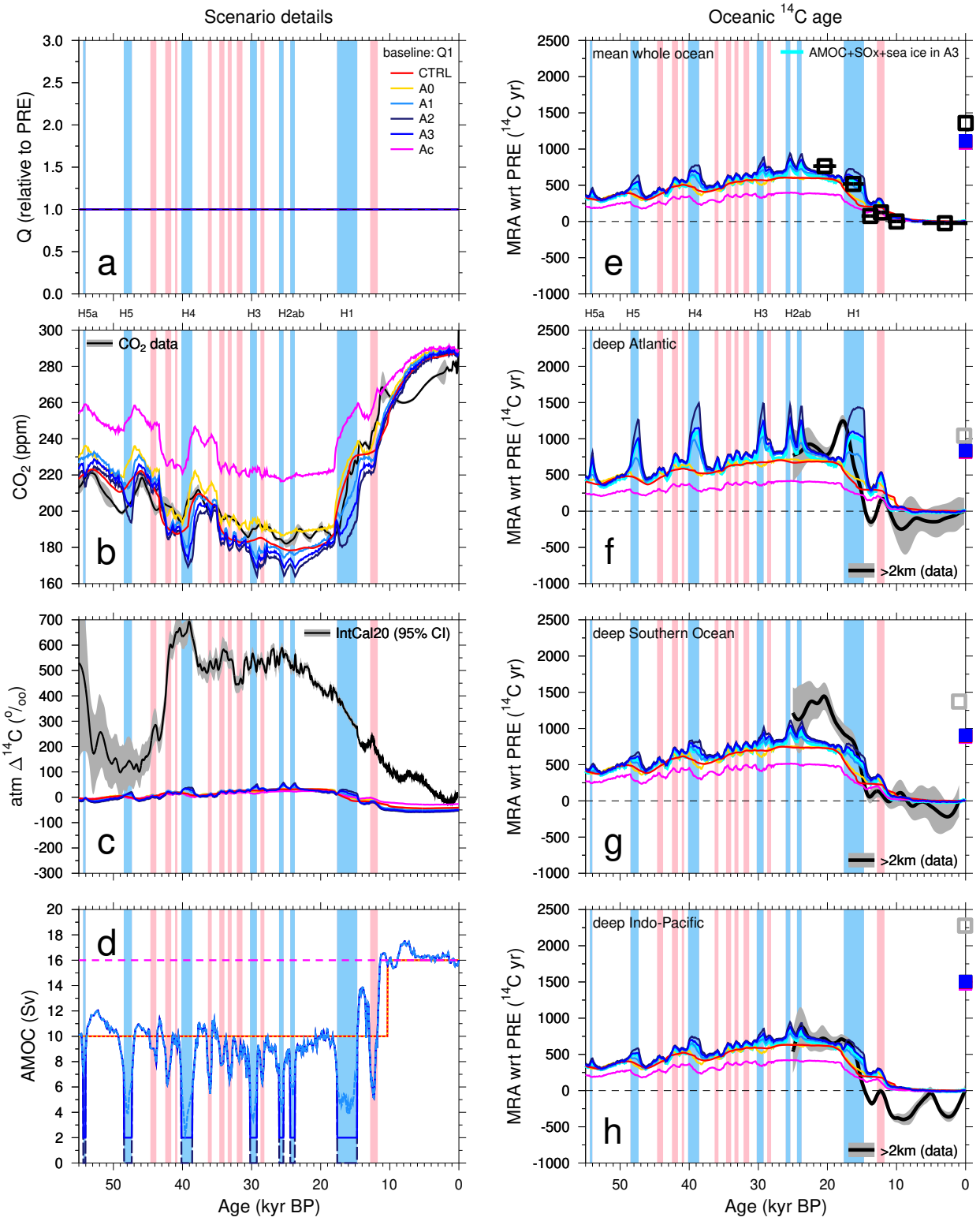

Figure S3: Main results for baseline Q1: ^{14}C production rate Q fixed at preindustrial value. (a): Q; (b) atmospheric CO_2 data (Köhler et al., 2017) vs. simulations; (c) atmospheric Δ^{14}C IntCal20 data (Reimer et al., 2020) vs. simulations; (d): prescribed AMOC in different scenarios. MRA with respect to preindustrial (PRE) for the (e) mean whole ocean; (f) deep Atlantic; (g) deep Southern Ocean; (h) deep Indo-Pacific. Black/grey for the last 25 kyr are reconstructions based on Skinner et al. (2023). Open squares in (e-h) mark the final values in the data time series from which the differences have been calculated (normally PRE), filled squares mark the PRE values in BICYCLE-SE. Light blue bares denote Heinrich events, pink bars non-Heinrich stadials.

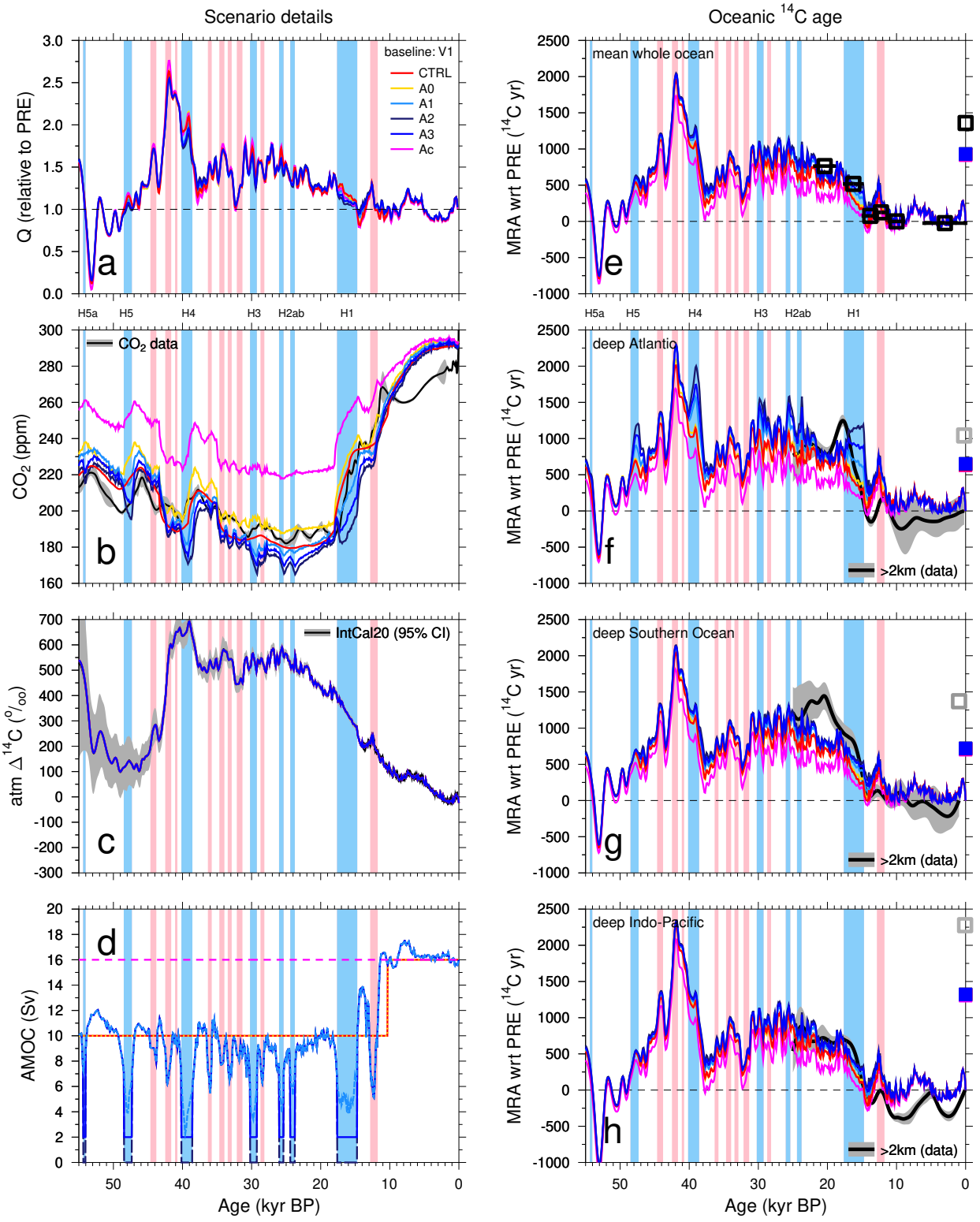

Figure S4: Main results for baseline V1: ^{14}C production rate Q calculated to meet atmospheric Δ^{14}C from IntCal20. (a): Q (400-yr running mean based on annual output); (b) atmospheric CO_2 data (Köhler et al., 2017) vs. simulations; (c) atmospheric Δ^{14}C IntCal20 data (Reimer et al., 2020) vs. simulations; (d): prescribed AMOC in different scenarios. MRA with respect to preindustrial (PRE) for the (e) the mean whole ocean; (f) deep Atlantic; (g) deep Southern Ocean; (h) deep Indo-Pacific. In (c) simulations results are prescribed to the mean of the reconstructions and therefore indistinguishable from the data. Black/grey for the last 25 kyr are reconstructions based on Skinner et al. (2023). Open squares in (e-h) mark the final values in the data time series from which the differences have been calculated (normally PRE), filled squares mark the PRE values in BICYCLE-SE. Light blue bares denote Heinrich events, pink bars non-Heinrich stadials.

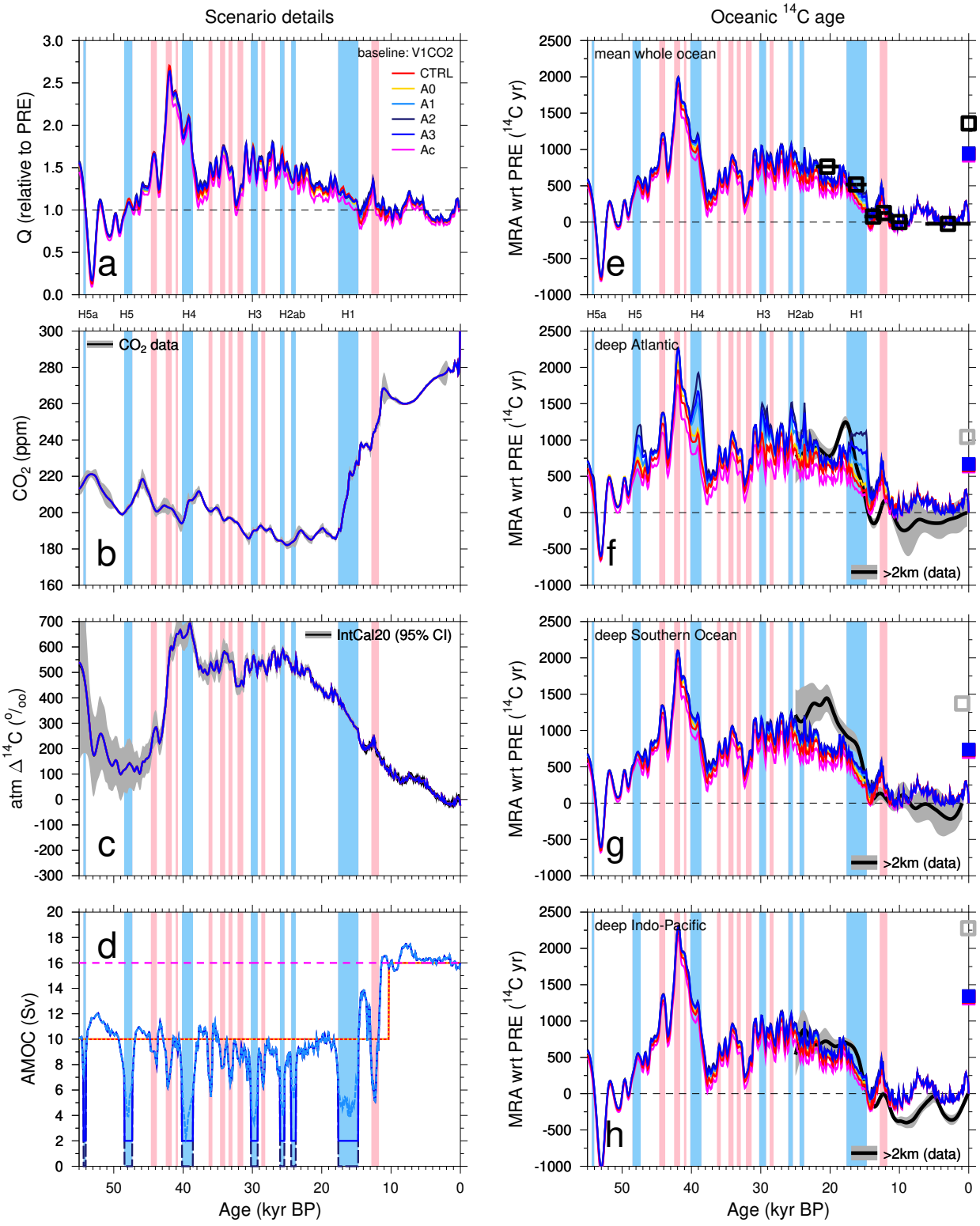

Figure S5: Main results for baseline V1CO2: ^{14}C production rate Q calculated to meet atmospheric Δ^{14}C from IntCal20 and atmospheric CO_2 prescribed from ice core data. (a): Q (400-yr running mean based on annual output); (b) atmospheric CO_2 data (Köhler et al., 2017); (c) atmospheric Δ^{14}C IntCal20 data (Reimer et al., 2020); (d): prescribed AMOC in different scenarios. MRA with respect to preindustrial (PRE) for the (e) the mean whole ocean; (f) deep Atlantic; (g) deep Southern Ocean; (h) deep Indo-Pacific. In (b,c) simulations results are prescribed to the mean of the reconstructions and therefore indistinguishable from the data. Black/grey for the last 25 kyr are reconstructions based on Skinner et al. (2023). Open squares in (e-h) mark the final values in the data time series from which the differences have been calculated (normally PRE), filled squares mark the PRE values in BICYCLE-SE. Light blue bares denote Heinrich events, pink bars non-Heinrich stadials.